

# **Manual for Seismic Resilient Construction and Retrofitting of Rammed earth and Stone masonry Houses**

## **Experimental results and data**

March 2023

Project on Evaluation and Mitigation of Seismic Risk for Composite Masonry Buildings in Bhutan  
in the framework of SATREPS Project



## Foreword

Guidelines for Seismic Resilient Houses of Rammed earth and Stone masonry - Experimental Results and Data Edition is the result of the six-year SATREPS (Science and Technology Research Partnership for Sustainable Development) project, which runs from April 2017 to the end of March 2023.

This document consists of 6 chapters. Chapter 1 provides a general background of the SATREPS project. Chapter 2 deals with the material properties especially rammed earth. Chapter 3 reports micro-tremor measurement and health monitoring on rammed earth traditional houses and stone masonry traditional houses. Chapter 4 covers a series of element tests on rammed earth and stone masonry. Chapter 5 provides the full-scale test on prototype traditional Bhutanese Rammed earth and Stone masonry houses having two-stories to clarify the effectiveness of proposed retrofitting and strengthening measures adopted in Chapter 4. Chapter 6 covers the shaking table tests.

I expressed my gratitude to JST (Japan Science and Technology Agency), JICA (Japan International Cooperation Agency), staff of the DoC (Department of Culture), MoHCA (Ministry of Home Affairs) and DES (Department of Engineering Services), MoWHS (Ministry of Works and Human Settlement).

I hope this experimental results and data is useful to guide for mitigating the seismic risk of rammed earth and stone masonry houses in Bhutan.

青木孝義

Takayoshi Aoki

Chief Advisor

Dean (Graduate School of Design and Architecture)

Nagoya City University

## List of Contents

<b>Chapter 1. Outline of the SATREPS Project .....</b>	<b>1</b>
1.1 Research background .....	1
1.1.1 Seismic Activity in Bhutan Since 1990.....	1
1.1.2 Traditional Masonry Constructions in Bhutan — Methods and Materials.....	2
1.1.3 Seismic Vulnerability of Traditional Masonry Buildings and the Need of Immediate Disaster Prevention Technology.....	2
1.2 Purpose of Study .....	3
1.3 Research System .....	4
<b>Chapter 2. Material Properties.....</b>	<b>5</b>
2.1 Basic mechanical characteristics of rammed earth .....	5
2.2 Efficacy of lime .....	7
2.3 Examination of material strength of rammed earth.....	8
2.4 Relationship between hydration rate and strength .....	12
2.5 Strength development with drying .....	13
2.6 Moisture content distribution from the surface to the inside of rammed earth.....	14
2.6.1 Construction of a moisture content measurement system using HI-800 .....	14
2.6.2 Estimated moisture content distribution of actual rammed earth structures in Bhutan.....	15
2.7 Corrosion resistance test of metal lath for reinforcing rammed earth .....	15
<b>Chapter 3. Micro-tremor measurement and health monitoring .....</b>	<b>18</b>
3.1 Target structure.....	18
3.2 Relationship between the heights of buildings and natural periods .....	21
3.3 Relationship between the heights of buildings and natural periods .....	22
3.4 Change of Natural Frequencies during the Full-scale Static Tests .....	23
3.5 Investigation of the vibration characteristics of the ground .....	25
3.6 Health Monitoring.....	27
<b>Chapter 4. Element Tests.....</b>	<b>31</b>
4.1 Static element test on rammed earth walls .....	31
4.1.1 Material and specimens .....	31
4.1.2 Test setup.....	33
4.1.3 Results .....	33
4.1.4 Finite element modelling of RE walls subjected to in-plane loading .....	35
4.2 Pull-down test of rammed earth walls .....	36
4.2.1 Material and specimens .....	36
4.2.2 Test setup.....	37
4.2.3 Results .....	37
4.2.4 Finite element modelling of RE walls subjected to out-of-plane loading .....	38
<b>Chapter 5. Static loading tests .....</b>	<b>40</b>

5.1 Test program .....	40
5.1.1 Materials.....	40
5.1.2 Test specimen details .....	41
5.2 Results and discussion.....	44
5.2.1 Micro-tremor measurements for dynamic characterization .....	44
5.2.2 Capacity curve .....	45
<b>Figure 5-5: (a) Capacity curves in each floor for both prototype unreinforced and retrofitted specimens, (b) Global capacity curves for both prototype and retrofitted specimens .....</b>	<b>45</b>
5.2.3 Damage observations and definition of the limit states .....	46
<b>Figure 5-7. Crack evolution for mesh-retrofitted rammed earth (RRE) specimen at different load levels and their respective limit states .....</b>	<b>50</b>
<b>Chapter 6. Shaking table tests .....</b>	<b>51</b>
6.1 Specimen configuration.....	51
6.2 Outline of shaking table tests .....	51
6.3 Results and discussion.....	52
<b>Acknowledgements .....</b>	<b>56</b>
<b>References.....</b>	<b>57</b>

## List of Figures

Figure 1-1. Historical earthquake source distribution in South Asia since 1960 .....	1
Figure 1-2. Earthquake events around Bhutan since 1990.....	2
Figure 1-3. Ramming of Rammed Earth Structure .....	3
Figure 1-4. Traditional Rammed Earth Buildings.....	3
Figure 1-5. Purpose of Project .....	3
Figure 1-6. Research System .....	4
Figure 2-1. Core drill .....	5
Figure 2-2. Sample Coring.....	5
Figure 2-3. Compressive strength testing .....	6
Figure 2-4. Tensile strength testing.....	6
Figure 2-5. Relationship between compressive strength and density .....	6
Figure 2-6. Relationship between Young's modulus and density.....	6
Figure 2-7. Relationship between tensile strength and density .....	7
Figure 2-8. Proportion of tensile strength to compressive strength .....	7
Figure 2-9. Relationship between compressive strength and density .....	8
Figure 2-10. Relationship between Young's modules and density .....	8
Figure 2-11. Relationship between tensile strength and density .....	8
Figure 2-12. Proportion of tensile strength to compressive strength .....	8
Figure 2-13. Development of compressive strength of rammed earth with cement added.....	9
Figure 2-14. Relationship between compressive strength of rammed earth and additive amount of cement.....	9
Figure 2-15. Relationship between compressive strength and accelerated carbonation time .....	10
Figure 2-16. Relationship between Young's modulus and compressive strength.....	10
Figure 2-17. Relationship between tensile strength and compressive strength.....	11
Figure 2-18. Relationship between compressive strength and number of compacted layers.....	11
Figure 2-19. Relationship between compressive strength and number of compacted times per layer .....	11
Figure 2-20. Relationship between dry density of rammed earth and moisture content of soil..	12
Figure 2-21. Development of compressive strength of rammed earth with varying water content of soil .....	13
Figure 2-22. Relationship between compressive strength and moisture content of soil .....	13
Figure 2-23. Development of compressive strength of rammed earth with varying drying temperature .....	13
Figure 2-24. Relationship between compressive strength and moisture content .....	13
Figure 2-25. The insertion electrodes .....	14
Figure 2-26. The inserted electrodes.....	14
Figure 2-27. The inserted electrodes.....	14
Figure 2-28. Measuring apparatus HI-800.....	14
Figure 2-29. Relationship between count value by electrical resistance measuring instrument and moisture content distribution of cut cores by absolute dry method .....	15
Figure 2-30. Relationship between estimated moisture content and depth from surface.....	15
Figure 2-31. Relationship between acceleration time and mass change rate .....	16
Figure 2-32. Relationship between acceleration time and tensile load capacity per wire.....	16
Figure 2-33. A shear test.....	17

Figure 2-34. Relationship between acceleration time and shear load capacity of the weld zone	17
Figure 3-1. Target of Rammed Earth Structures (External view)	20
Figure 3-2. Target of Stone Masonry Structures (External view and abbreviate plan of the top floor)	21
Figure 3-3. Relationship between natural periods and the heights of buildings	22
Figure 3-4. Relationship between natural periods and aspect ratio (Width/Height)	23
Figure 3-5. Location of microtremor measurement near the Babesa House No.2 (Google Earth Map)	25
Figure 3-6. Location of microtremor measurement at Tshenkher settlement of Talung village in the Haa Dzongkhag (Google Earth Map)	26
Figure 3-7. Microtremor measurement of ground at Tshenkher settlement of Talung village in the Haa Dzongkhag	26
Figure 3-8. H/V spectral ratio of the ground	27
Figure 3-9. Monitoring of Rammed Earth building in Debsi, Thimphu	27
Figure 3-10. Measuring position and measuring condition	28
Figure 3-11. Observed Accelerations and Temperature	29
Figure 3-12. Observed Earthquakes	29
Figure 3-13. Monitoring of Stone Masonry building in Samcholing, Trongsa	30
Figure 4-1. Failure mechanism in RE buildings []	31
Figure 4-2: (a) Ramming to desired thickness; (b) Complete specimen	32
Figure 4-3. Compaction difference between the wallettes	32
Figure 4-4. Strengthening details: (a) Fixation of mesh and screws; (b) Final view after plastering specimen	32
Figure 4-5. Test set up: (a) Compression test; (b) Shear test	33
Figure 4-6. Compressive stress-strain curve of unreinforced wallettes	34
Figure 4-7. Shear load-displacement curve of unreinforced wallettes	34
Figure 4-8. Shear strength of RE wallettes subjected to various vertical stresses	34
Figure 4-9. Shear load-displacement curve of strengthened wallettes: (a) 3-months dried; (b) 12-months dried	34
Figure 4-10. Typical failure patterns of RE wallettes observed under compression loading	35
Figure 4-11. Typical failure patterns of RE wallettes observed under shear loading	35
Figure 4-12. Material model adopted in FE Modelling	35
Figure 4-13. Failure mode observed in FE model: (a) unreinforced wallet; (b) Strengthened wallet	36
Figure 4-14. Results of sensitivity analysis	36
Figure 4-15. Specimen showing strengthening details: (a) Mesh-RE; (b) Timber-RE; (c) New-RE-A; (d) New-RE-B; (e) RC wedges and RC dowels inside formwork	37
Figure 4-16. Test setup: (a) Overall view of pull-down test; (b) Location of transducers	37
Figure 4-17. Load–displacement relationship at: (a) Top facade; (b) Mid facade; (c) Top of transverse wall	38
Figure 4-18. Final failure modes of all RE walls under out-of-plane loading	38
Figure 4-19. Experiment and FE results	38
Figure 4-20. Failure modes observed for: (a) FE-macro; (b) FE-micro	39
Figure 5-1. Material characterization tests for mesh retrofitting component: (a) Test coupons epoxy-bonded at the ends to steel plates, (b) Test set–up with clevis type grips, (c) Tensile stress versus strain plots for tensile coupon tests of M–Mesh, (d) Typical failure mode at the end of coupon test	41

Figure 5-2. Prototype retrofitted rammed earth building specimen (RRE).....	42
Figure 5-3. Retrofitting work process: (a) Placement and anchorage of mesh, (b) Application of cement slurry as pretreatment, (c) Cement plastering, (d) Wooden brace for floor rigidity, (e) Final specimen after retrofitting .....	43
Figure 5-4: (a)Test set-up and instrumentation; (b) Actual and target storey drifts .....	44
Figure 5-5: (a) Capacity curves in each floor for both prototype unreinforced and retrofitted specimens, (b) Global capacity curves for both prototype and retrofitted specimens.....	45
Figure 5-6. Crack evolution for unreinforced rammed earth (URE) specimen at different load levels and their respective limit states.....	49
Figure 5-7. Crack evolution for mesh–retrofitted rammed earth (RRE) specimen at different load levels and their respective limit states.....	50
Figure 6-1. Plan of specimen .....	51
Figure 6-2. Reinforcement with wire mesh.....	51
Figure 6-3. Example of time history .....	52
Figure 6-4. Installation of specimen .....	52
Figure 6-5. Example of acceleration spectrum .....	52
Figure 6-6. Acceleration response factor .....	53
Figure 6-7. Crack patterns after tests (Short direction).....	54
Figure 6-8. Crack patterns after tests (Long direction) .....	54
Figure 6-9. Change of natural frequencies.....	55

## List of Tables

Table 2-1. Mixing proportion of rammed earth .....	7
Table 2-2. Mechanical properties of rammed earth .....	8
Table 3-1. Overview of Rammed Earth buildings to be measured and list of measurement results .....	18
Table 3-2. Overview of Stone Masonry buildings to be measured and list of measurement results .....	18
Table 3-3. Overview of Stone Masonry buildings to be measured and list of measurement results .....	24
Table 3-4. Acceleration Amplification Ratio. Gal in parentheses. ....	30
Table 4-1. Experimental and FE results.....	36
Table 5-1. Material characterization of rammed earth block .....	40
Table 5-2. Results from micro-tremor measurements .....	45
Table 5-3. Test results for the prototype unreinforced and retrofitted specimens.....	46
Table 5-4. Limit states for rammed earth building .....	47



# Chapter 1. Outline of the SATREPS Project

## 1.1 Research background

### 1.1.1 Seismic Activity in Bhutan Since 1990

Bhutan, along with India, Pakistan and Nepal, lies in the Himalayan range with one of the world's most active earthquake occurrences (Figure 1-1). The frequent earthquakes around this region occur as a result of the collision of the Indian Plate and the Eurasian Plate along the fault interfaces between these plates.

The most recent earthquake to occur in this India-Eurasia collision zone is Gorkha earthquake in central Nepal, with magnitude M7.8 on April 25, 2015 resulting in 8,800 casualties with damages spread across the country. Further, there was Kashmir earthquake of magnitude M7.6 in western Pakistan on year 2005 with 90,000 deaths in the region. Bhutan, on the other hand, has not experienced any major earthquake exceeding magnitude M7 during the 20th century (Figure 1-2). The last major earthquake close to Bhutan was Shillong earthquake measuring M8.3 on year 1897, that occurred in Assam region of India close to the southern part of Bhutan. An earthquake of magnitude M6.1 occurred on September 2009 with Bhutan as its epicenter that resulted in first human casualty due to earthquake event after the establishment of the Kingdom of Bhutan in 1907. Furthermore, in September, 2011, India-Sikkim earthquake of magnitude M6.9 resulted in significant damage to the existing infrastructures in Paro, the western part of Bhutan. These recent events show a high probability of another strong earthquake to occur close to the Bhutan Himalayan region.

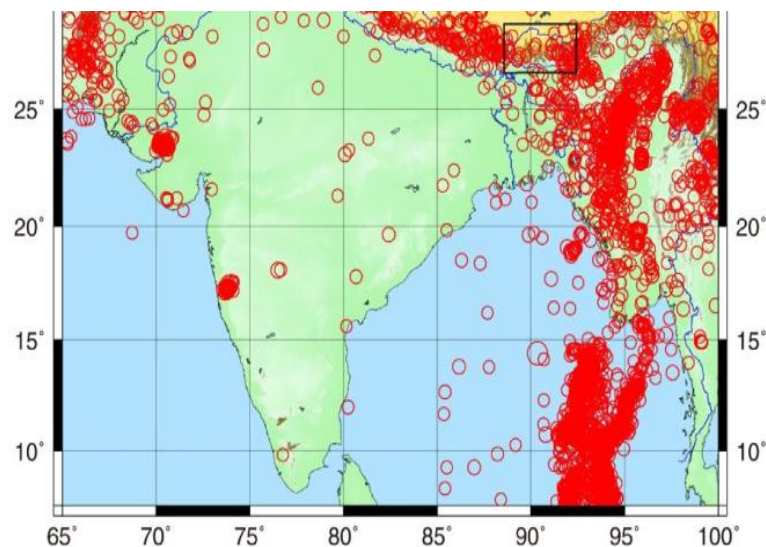


Figure 1-1. Historical earthquake source distribution in South Asia since 1960  
(Earthquakes of magnitude M5 or mor are plotted from the ISC Catalog)

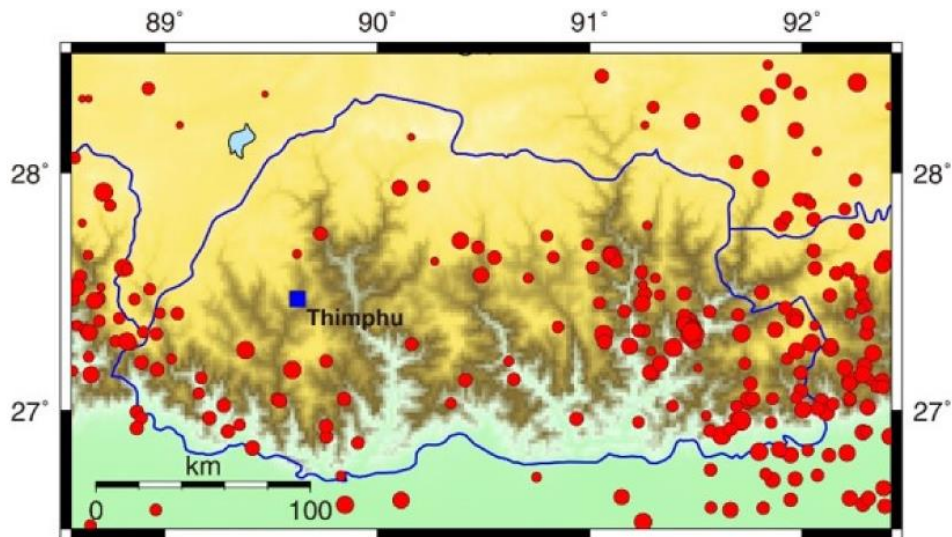


Figure 1-2. Earthquake events around Bhutan since 1990

(Red dots include all the earthquakes recorded in the ISC Catalog for the enlarged rectangular region of Figure at Figure 1-1)

### 1.1.2 Traditional Masonry Constructions in Bhutan — Methods and Materials

The traditional architectural construction of Bhutan follows different construction practices across the country's geography. The western region has traditional rammed earth construction, and the eastern region has mostly stone masonry structures. The traditional rammed earth construction includes a foundation made of stone block masonry, above which the rammed earth walls are constructed. The normal rammed earth private house building is usually two to three stories high, where the first floor is used as a space for live stocks or warehouses. This floor is usually a closed space with very few openings. The second and third floors are living spaces with walls, floors and inner pillars/posts made of wood or mud. The timber roofing at roof rests on the wooden horizontal beams on top of the walls. Traditional constructions usually have roofs with long plate rocks. The construction materials of rammed earth walls involve red clay/soil with small pebbles, locally available in the nearby area of the construction site. The soil is carried in bags to the construction site and poured inside the space within the wooden formwork, followed by ramming of the soil until the upper soil layer becomes smooth, polished and sufficiently hard (Figure 1-3). After the ramming of one-layer, new soil is poured over, followed by ramming. A similar procedure is repeated for about 7-8 layers. After one block is completed, the wooden formwork is removed and installed at the next construction place.

### 1.1.3 Seismic Vulnerability of Traditional Masonry Buildings and the Need of Immediate Disaster Prevention Technology

The reinforced concrete building and brick masonry building constructions are commonly seen in urban areas of Bhutan, in the capital city of Thimphu. However, outside the urban development, the majority of the population lives in private buildings comprising traditional rammed earth buildings and stone block masonry structures (Figure 1-4). These traditional buildings are particularly vulnerable

to earthquake events, as seen after the earthquakes in the eastern region of Bhutan (September 21, 2009, M6.1) and the India-Nepal border area (September 18, 2011, M6.9). There is a general awareness among the people in Bhutan regarding measures to improve the seismic performance of existing structures. However, at the present condition, there are no guidelines available for the traditional Bhutanese buildings, and hence, they tend to follow existing overseas guidelines such as Indian Standards. Here, to mitigate the possible future earthquake disaster in Bhutan, our work is focused on the development and dissemination of effective earthquake-resistant guidelines for traditional buildings based on experimental work and structural analysis and further knowledge gained through seismic observation and social and economic survey of Bhutan. This will be an indispensable support to scientific and technological development as a whole.

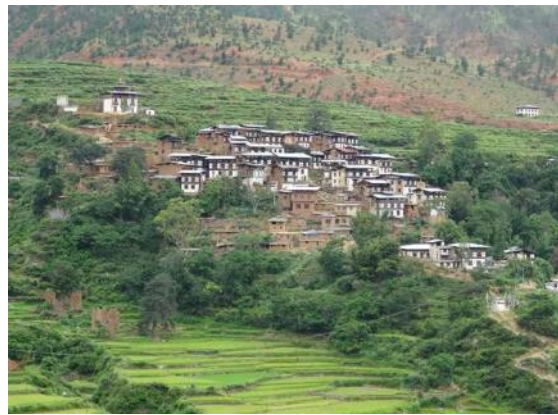


Figure 1-3. Ramming of Rammed Earth Structure Figure 1-4. Traditional Rammed Earth Buildings

## 1.2 Purpose of Study

The purpose of this project is shown in the illustration (Figure 1-5).

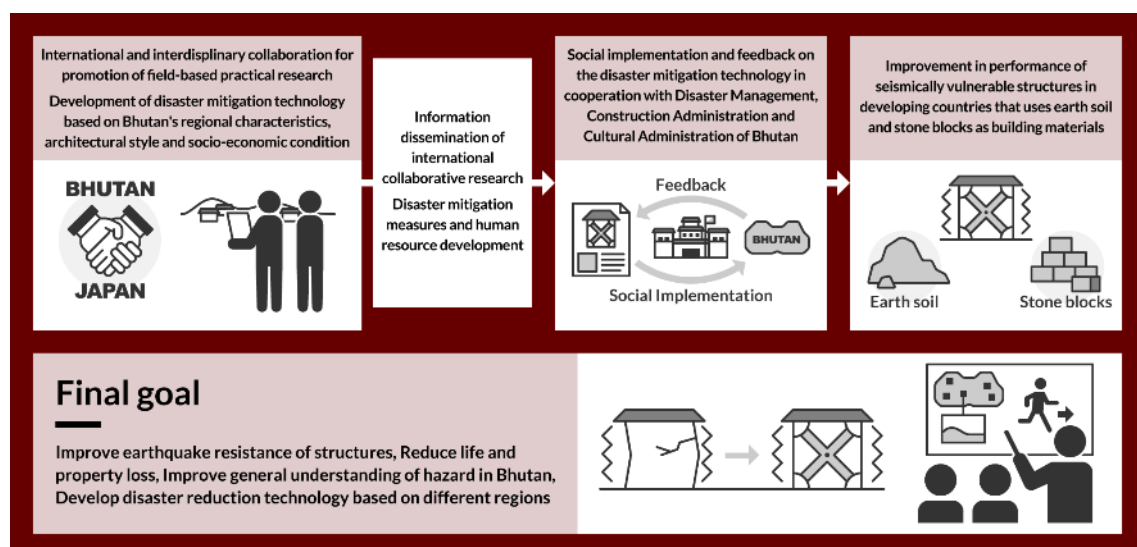


Figure 1-5. Purpose of Project

### 1.3 Research System

The research system of this project is shown in the illustration (Figure 1-6).

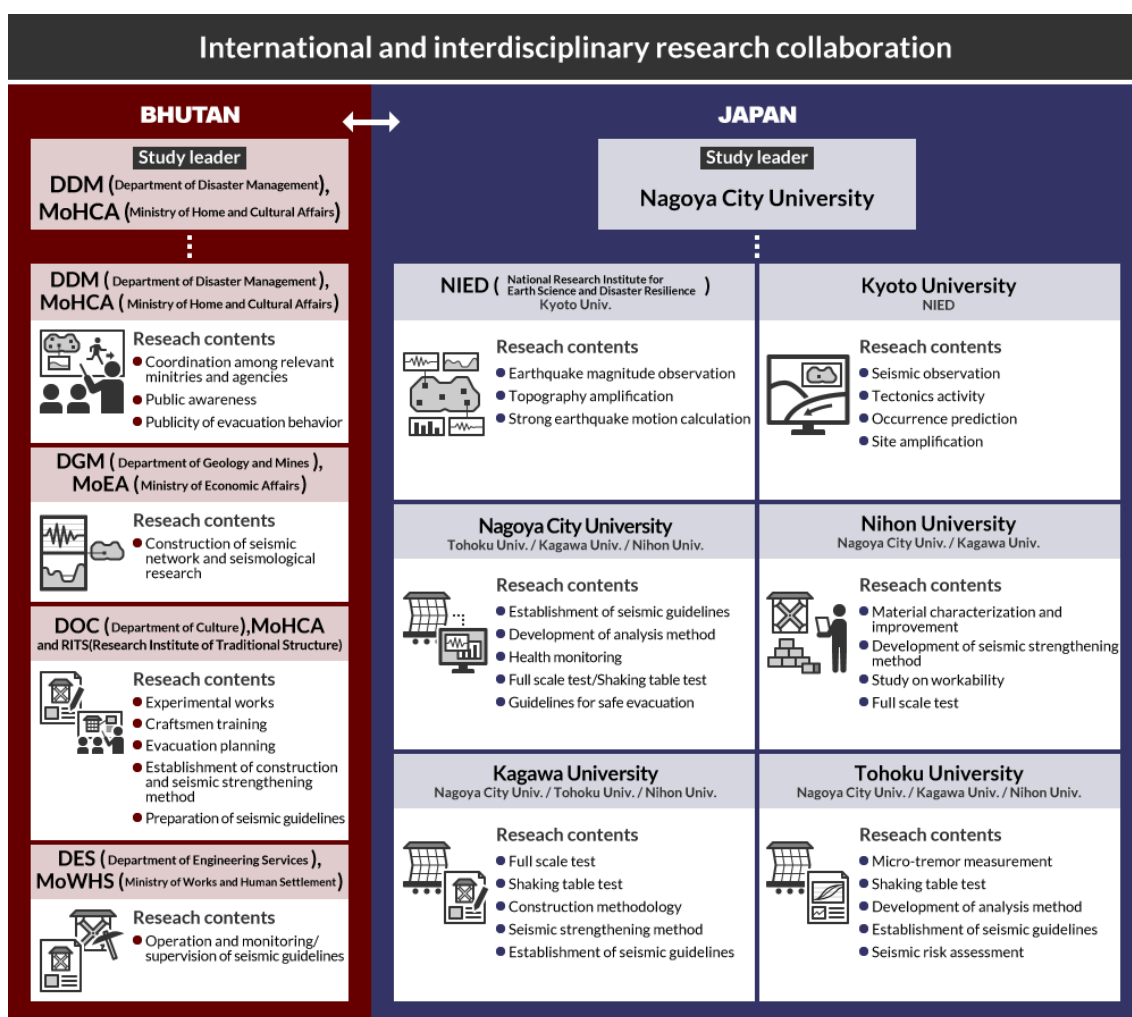


Figure 1-6. Research System



## Chapter 2. Material Properties

### 2.1 Basic mechanical characteristics of rammed earth

For structural calculation of new rammed earth structures and seismic evaluation of existing rammed earth structures, material properties such as compressive strength, tensile and shear strength, and Young's modulus of rammed earth should be obtained. In order to grasp mechanical characteristics of rammed earth and to clarify the effectiveness of use of lime for rammed earth, compressive strength testing on two types of rammed earth test samples were conducted: one type from the actual structures and the others collected from rammed earth blocks prepared on the site [1]. It is difficult to cut rectangular form of rammed earth sample. Therefore, by using a core drill with a diameter on 100mm (DD120 Hilti Corporation) shown in Figure 2-1, coring of the sample about 100-200mm long was conducted (Figure 2-2).



Figure 2-1. Core drill



Figure 2-2. Sample Coring

Each test sample was judged if it was suitable for being used for compressive strength testing (Figure 2-3) or for tensile strength testing (Figure 2-4) according to its length and surface crack. In the case of compressing strength testing, test pieces that have approximately twice the length of their diameters. Test samples were irregularly shaped because of processing difficulties; therefore, samples were collected so as to ensure that both top and bottom surfaces were compressed flat and capped with plaster.



Figure 2-3. Compressive strength testing



Figure 2-4. Tensile strength testing

Figure 2-5 shows the relationship between compressive strength and density and Figure 2-6 shows the relationship between Young's modulus and density respectively. Specimen 3BU was collected from the rammed earth block that was made of only red soil and water, based on the mixing proportion used by Bhutanese craftsmen and then cured for three months. Specimen 3JU was collected from the rammed earth block that was made of red soil, yellow soil and water, based on the mixing proportion suggested by Mr. Takashina, which has a ratio of four parts red soil to one-part yellow soil. Compared to the rammed earth blocks made by Bhutanese craftsmen, the rammed earth block from Mr. Takashina had low water content and was rammed more with the ramming process taking relatively long time. Comparing the test results of 3BU-H and that of 3JU-H, there is little difference in compressive strength but Young's modulus of 3JU-H is about 1.2 times higher than the 3BU-H. The measured values are mostly distributed in around these two areas: one of which has the density of around 1700-1800 [kg/m<sup>3</sup>] with compressive strength of approximately 0.5 – 0.9 [MPa] and the other has the density of about 1900-2000 [kg/m<sup>3</sup>] with compressive strength of approximately 1.4 – 1.7 [MPa]. The latter material is more suitable for rammed earth structures.

Figure 2-7 shows the relationship between tensile strength and density respectively. The measured values are mostly distributed in around the areas one of which has the density of around 1600-1800 [kg/m<sup>3</sup>] with the tensile strength of approximately 0.04 – 0.07 [MPa]. Figure 2-8 summarizes the ratios [c/t] of compressive strength to tensile strength. Excluding the case where there is only one specimen, the values of ratios c/t fall in the range of 7.02 to 14.5.

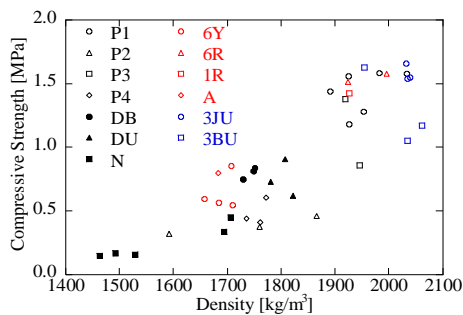


Figure 2-5. Relationship between compressive strength and density

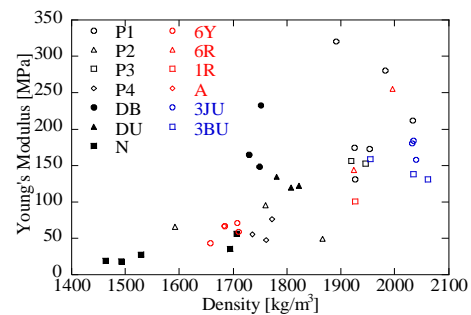


Figure 2-6. Relationship between Young's modulus and density

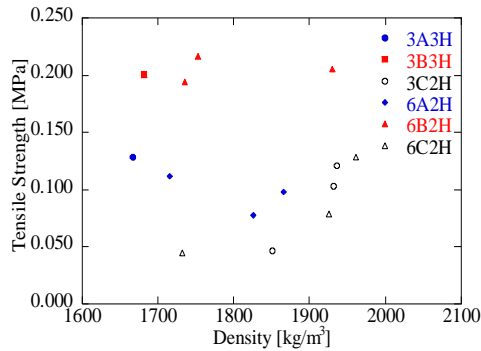


Figure 2-7. Relationship between tensile strength and density

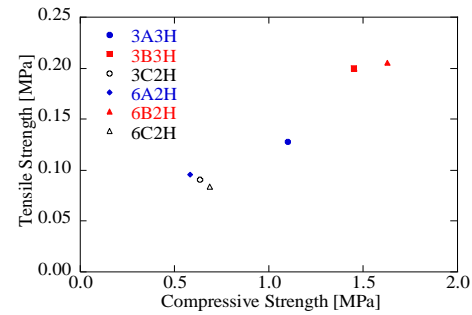


Figure 2-8. Proportion of tensile strength to compressive strength

## 2.2 Efficacy of lime

When the soil is not suitable material for the construction of rammed earth structure, some additives such as lime are necessary to improve mechanical properties of rammed earth. The specimens were collected from the rammed earth blocks made by Bhutanese craftsmen with three different mixing ratios of local gravel, red soil and lime. Mixing ratios of gravel, red soil and lime are: Ratio A is 1:8:1, Ratio B is 1:5:2 and Ratio C is 1:8:0 as shown in Table 2-1. Since the collecting locations of red soil were different depending on executed periods, it was confirmed that the grain size distributions of these two types of red soil are almost the same through sieving testing.

Table 2-1. Mixing proportion of rammed earth

Ingredients	Type A	Type B	Type C
Gravel	1	1	1
Red clay	8	5	8
Slaked lime	1	2	0

Figure 2-9 shows the relationship between compressive strength and density and Figure 2-10 shows the relationship between Young's modulus and density respectively. There are tendencies that as for the density the value increases from mixing ratio A, B to C in ascending order and regarding both compressive strength and Young's modulus the values increase from mixing ratios C, B to A in the reverse order (Table 2-2).

Figure 2-11 shows the relationship between tensile strength and density. As for the density the value of the ones created based on the mixing ratio A and the one on the mixing ratio B are on the same level, which is smaller than the one on the mixing ratio C. Regarding tensile strength, the value increase from mixing ratios C, B to A in order (Table 2-2).

Figure 2-12 summarizes the ratios  $[c/t]$  of compressive strength to tensile strength. The values of ratios  $c/t$  fall in the range of 6.11 to 8.59.

Table 2-2. Mechanical properties of rammed earth

Ingredients	Type A	Type B	Type C
Density[kg/m <sup>3</sup> ]	1827	1813	1965
Compressive strength[MPa]	0.791	1.558	0.662
Tensile strength[MPa]	0.104	0.204	0.087

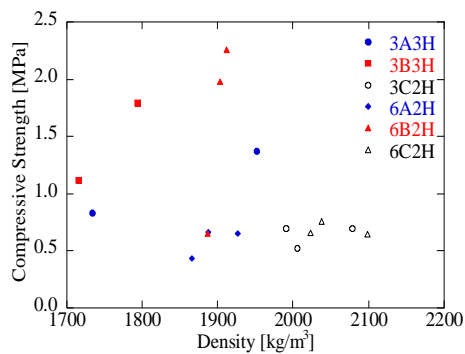


Figure 2-9. Relationship between compressive strength and density

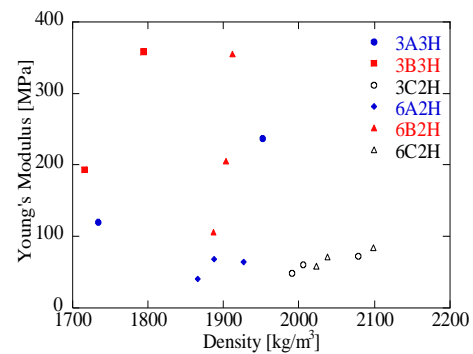


Figure 2-10. Relationship between Young's modules and density

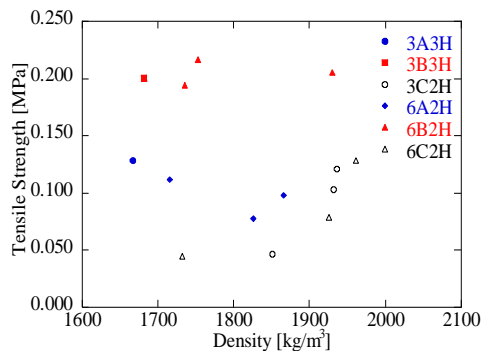


Figure 2-11. Relationship between tensile strength and density

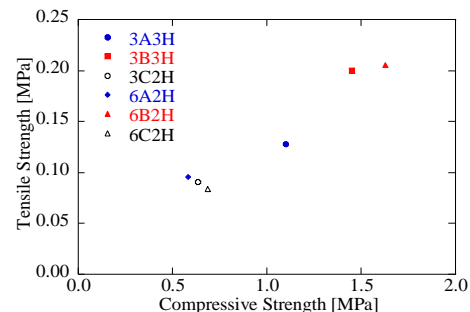


Figure 2-12. Proportion of tensile strength to compressive strength

## 2.3 Examination of material strength of rammed earth

In order to improve the seismic performance of rammed earth that is constructed by compacting soil, the strength properties of rammed earth materials were investigated from the viewpoint of improving and improving them.

Figure 2-13 shows the relationship between material age and compressive strength. In soil alone, the strength of the non-dried (sealed) specimens remains constant even after aging, while the strength of the dried (air-cured) specimens increases, suggesting that the strength enhancement mechanism of



rammed-earthen. It is found to be dry. Even with the addition of cement, the development of strength in air curing was almost the same as when no cement was added.

On the other hand, in the case of sealed curing, the strength increased due to the hydration of cement, and as shown in Figure 2-14, the strength increased with the addition of cement. These results indicate that the addition of cement is not effective on the surface layer of rammed earth, but it can be expected to be effective in increasing the strength of the slowly drying interior.

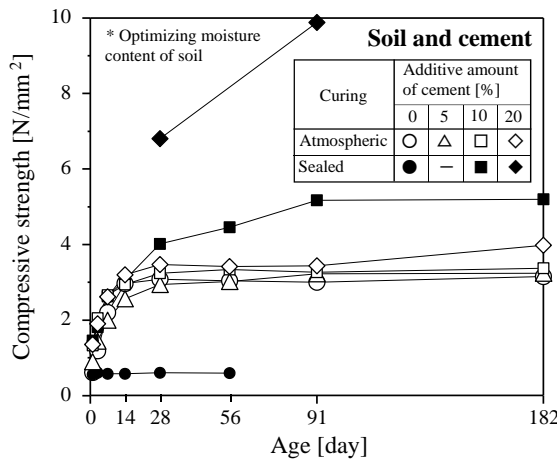


Figure 2-13. Development of compressive strength of rammed earth with cement added

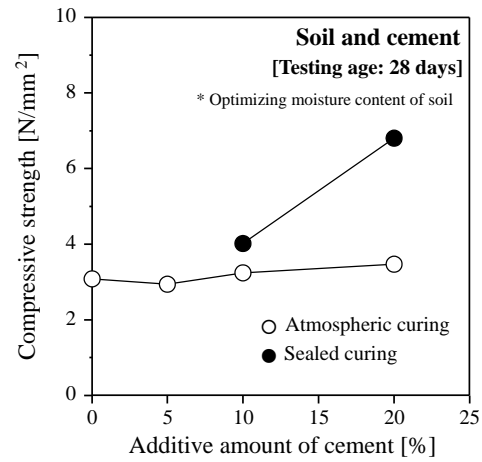


Figure 2-14. Relationship between compressive strength of rammed earth and additive amount of cement

Figure 2-15 shows the relationship between carbonation age and compressive strength of specimens to which slaked lime was added. It was found that the addition of slaked lime is not effective as a strength improvement measure, because the increase in strength is small even when the amount added is 20%.

Figure 2-16 shows the relationship between compressive strength and static elastic modulus. The static modulus of elasticity was found to be one to two orders of magnitude lower than that of concrete of general strength level. It was  $0.34 \times 10^3 \text{ N/mm}^2$  for the 182-day-old soil specimen, and  $3.1 \times 10^3 \text{ N/mm}^2$  for the 10% cement sealed specimen. Similar to concrete, it was confirmed in this test specimen that the static elastic modulus increases as the compressive strength increases.

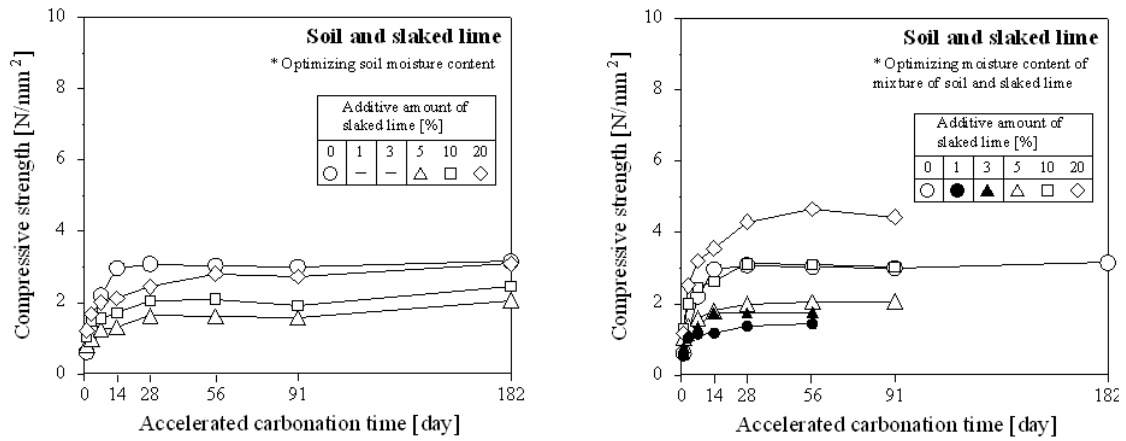


Figure 2-15. Relationship between compressive strength and accelerated carbonation time

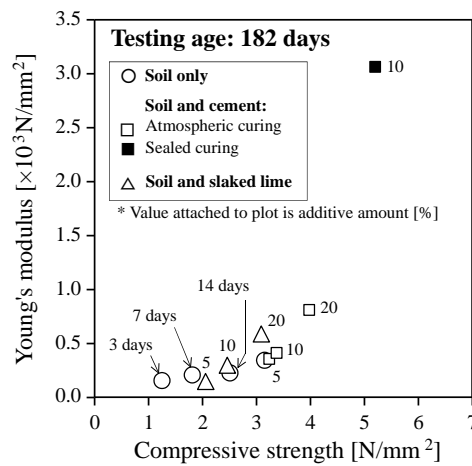


Figure 2-16. Relationship between Young's modulus and compressive strength

Figure 2-17 shows the relationship between compressive strength and tensile strength. The tensile strength of the specimens was 1/12 to 1/9 of the compressive strength, which is the same as that of ordinary concrete.

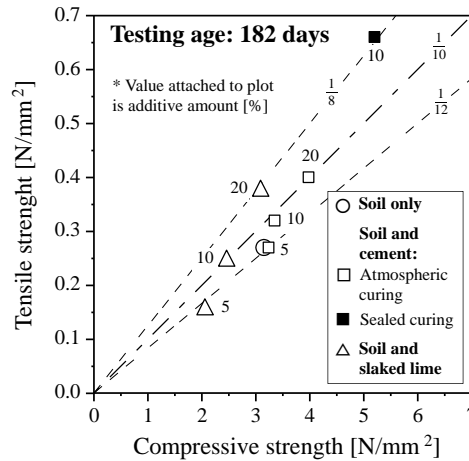


Figure 2-17. Relationship between tensile strength and compressive strength

Figure 2-18 shows the relationship between the number of tamped layers and the compressive strength. The compressive strength of the soil-only specimen had a maximum value with respect to the number of tamped layers. In the range of the experiment, it has a maximum value with 6 layers, which is 1.5 times higher than that with 4 layers.

Figure 2-19 shows the relationship between the number of compactions and the compressive strength. The compressive strength also has a maximum value with respect to the number of times of tamping, and in the range of the experiment, the maximum value was 1.4 times that at 25 times compared to 15 times. The compressive strength of the cement-added sealed specimens increased as the number of tamped layers increased. The relationship between the number of times of tamping and the compressive strength of the cement-added sealed test specimens was large at 15 times, but remained constant at 25 times or more.

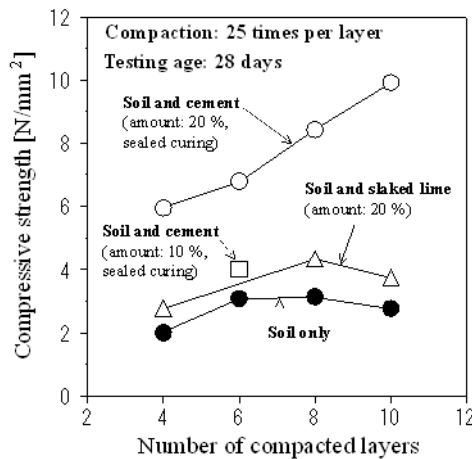


Figure 2-18. Relationship between compressive strength and number of compacted layers

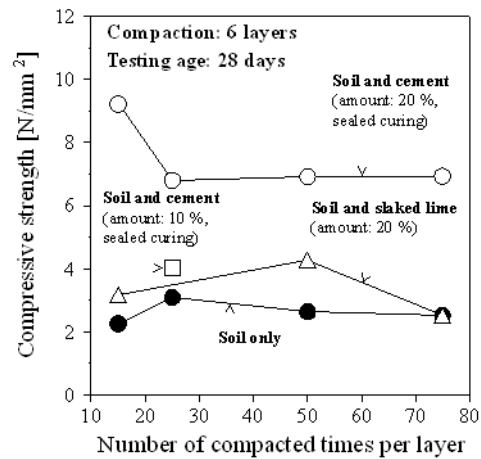


Figure 2-19. Relationship between compressive strength and number of compacted times per layer

## 2.4 Relationship between hydration rate and strength

Generally speaking, the higher the density of the material, the higher the strength. In order to confirm whether there is a similar tendency for rammed earth, the relationship between water content and strength was examined.

According to Figure 2-20, in the material used, the hydration rate at which the dry density was approximately maximum was about 15%.

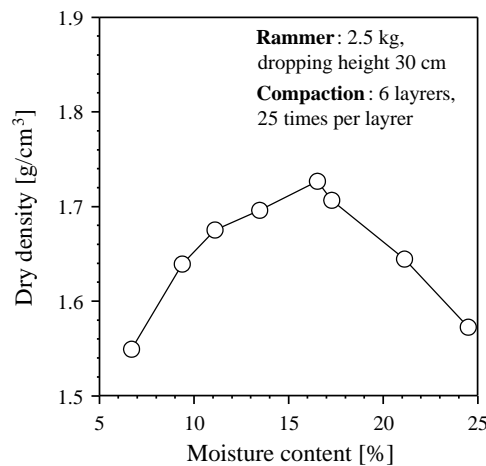


Figure 2-20. Relationship between dry density of rammed earth and moisture content of soil

Figure 2-21 shows changes in compressive strength depending on water content. Figure 2-22 shows this result as a relationship between water content and strength. Specimens with 15% hydration showed the highest strength at all ages. The 182-day strength difference between the 7% and 15% water content specimens was  $0.96 \text{ N/mm}^2$ , which is a large difference for rammed earth materials with low strength levels.

It was confirmed that not only the density but also the strength of the specimen with the optimum hydration ratio in terms of density, as shown in Figure 2-13, was maximized.

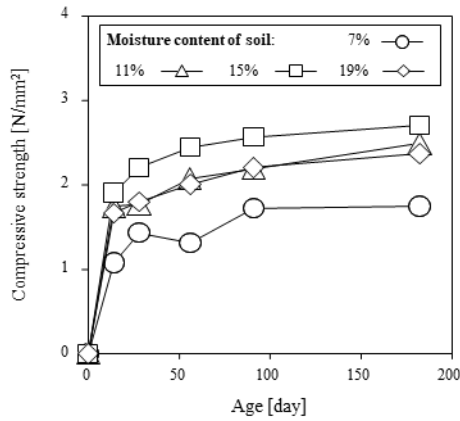


Figure 2-21. Development of compressive strength of rammed earth with varying water content of soil

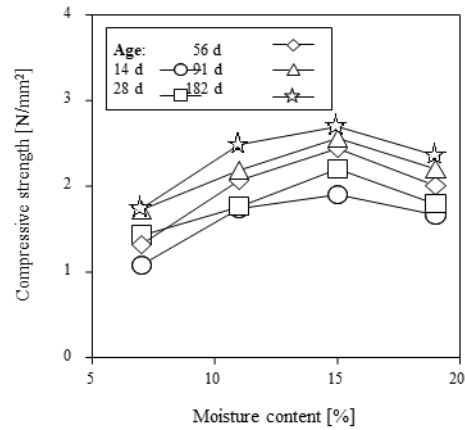


Figure 2-22. Relationship between compressive strength and moisture content of soil

## 2.5 Strength development with drying

Figure 2-23 shows changes in compressive strength during drying. The strength of the specimens dried in a room of 5°C showed the lowest value at all ages, and the strength of the specimens other than 35°C increased as the drying temperature increased. The strength of specimens dried at 27°C and 35°C from 14th day increased rapidly between 14th day and 28th day.

Figure 2-24 shows the relationship between water content and compressive strength. It can be seen that there is a good correlation between the water content and compressive strength regardless of the drying temperature.

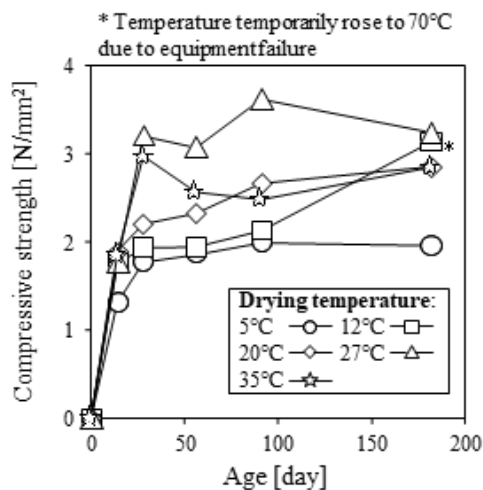


Figure 2-23. Development of compressive strength of rammed earth with varying drying temperature

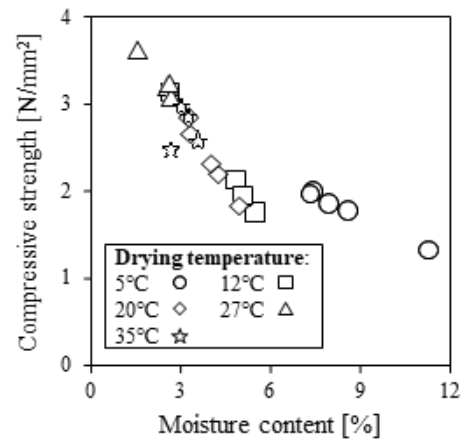


Figure 2-24. Relationship between compressive strength and moisture content

## 2.6 Moisture content distribution from the surface to the inside of rammed earth

### 2.6.1 Construction of a moisture content measurement system using HI-800

To test the moisture content distribution in building materials, the core is first cut dry and then cut by depth from the surface. Absolutely dry each at 105°C and calculate the moisture content. However, with this method, it is difficult to dry cut the core layer by layer. Therefore, in measuring the moisture content distribution of rammed earth, we investigated a method of electrically grasping it using the insertion electrodes shown in Figure 2-25. Using an actual rammed-earth structure that was built more than a year ago in Bhutan and a simulated rammed-earth block made for laboratory use, the electrical property values were measured by inserting electrodes and by dry core extraction and cutting. The relationship of moisture content was obtained.



Figure 2-25. The insertion electrodes

First, drill 10 mm diameter holes parallel to the rammed earth with a center-to-center distance of 5 cm. As shown in Figure 2-26 and Figure 2-27, electrodes with diameter of 10 mm were inserted, and the electrical characteristics of the electrode were measured using HI-800 (Figure 2-28) commercially available in Japan. The count value is inversely proportional to the electrical resistance between the electrodes.

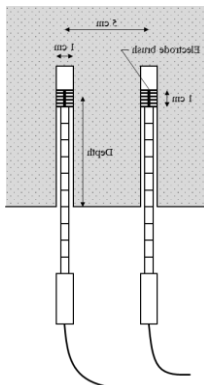


Figure 2-26. The inserted electrodes



Figure 2-27. The inserted electrodes



Figure 2-28. Measuring apparatus HI-800

Figure 2-29 shows the relationship between the count value obtained by the insertion electrode and the moisture content obtained by the core-cutting absolute dry method. The count value and the moisture content obtained by the core cutting absolute dry method correspond well, and we decided to consider the approximate line in the figure as the calibration curve.

## 2.6.2 Estimated moisture content distribution of actual rammed earth structures in Bhutan

Estimated moisture content distribution of actual rammed earth structures in Bhutan. Figure 2-30 shows the estimated water content calculated from the electrode count values using the approximate line (calibration curve) in Figure 2-29. The moisture content is lower in the surface layer, and the change is moderate in the layer deeper than 4 cm.

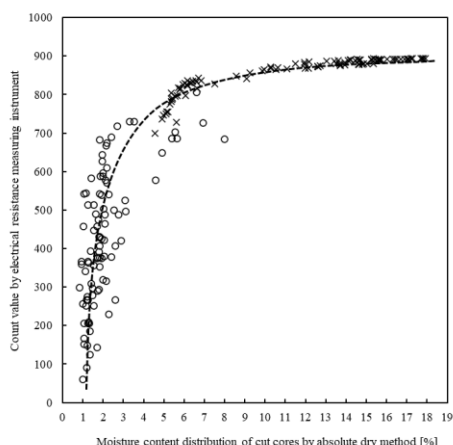


Figure 2-29. Relationship between count value by electrical resistance measuring instrument and moisture content distribution of cut cores by absolute dry method

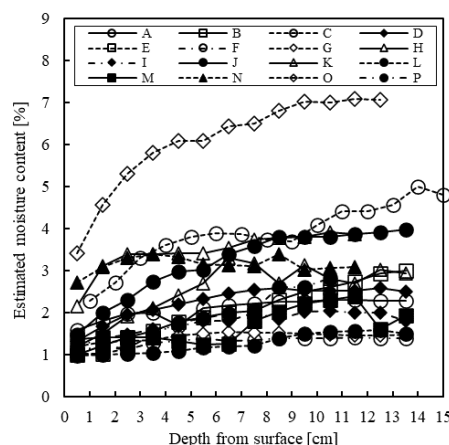


Figure 2-30. Relationship between estimated moisture content and depth from surface

Except for ruined structures, it was found that the moisture content distribution generally decreased as the years passed after the construction of rammed earth. However, building A, which is believed to be over 100 years old, had a high moisture content.

In Building A, when we examined the difference between sunny and shaded areas, the moisture content distribution in sunny areas was clearly lower than that in shaded areas.

For ruins, which were exposed, the results were different.

## 2.7 Corrosion resistance test of metal lath for reinforcing rammed earth

A corrosion resistance test of metal lath for reinforcing rammed earth was conducted according to JIS A 5505 Metal laths and JIS Z 2371 Methods of salt spray testing. The sprayed salt water concentration is  $50 \text{ g/L} \pm 5 \text{ g/L}$ .

Figure 2-31 shows the relationship between acceleration time and mass change rate. The mass after 648 hours of acceleration was the smallest for silver (thin), which has the smallest diameter, at 66.5%, and the mass for brown, which has the largest diameter, was 84.2%, and silver (thick) was 96.1%.

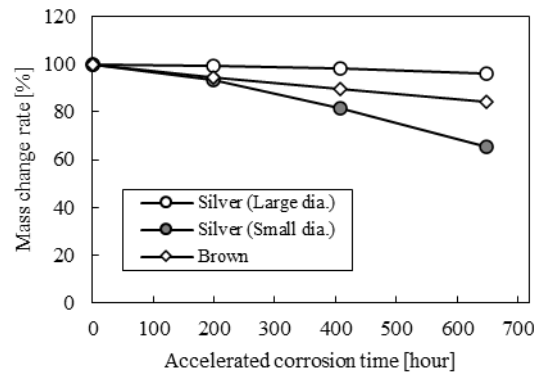


Figure 2-31. Relationship between acceleration time and mass change rate

Figure 2-32 shows the relationship between acceleration time and tensile load capacity per wire. Silver (thick) was little change after 648 hours of acceleration. Silver (thin) and brown became smaller as the acceleration time passed. The change was greater in brown than in silver (thin).

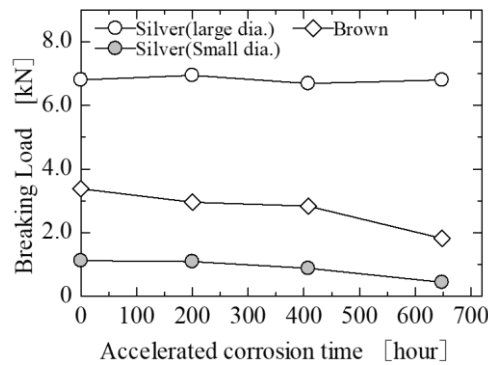


Figure 2-32. Relationship between acceleration time and tensile load capacity per wire

In addition, as shown in the Figure 2-33, a shear test was performed on the weld. Figure 2-34 shows the relationship between acceleration time and shear load capacity of the weld zone. Silver (thick) can be said that there is not much change after 648 hours of acceleration.

Silver (thin) and brown of shear load capacity of the weld zone decreased with the passage of acceleration time, similar to the tensile load of the wire rod, the change was larger in brown than in silver (thin).



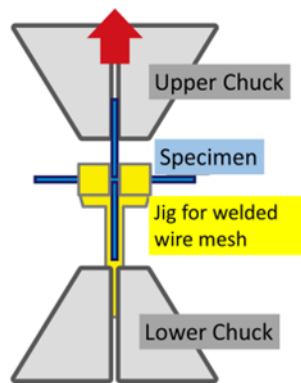


Figure 2-33. A shear test

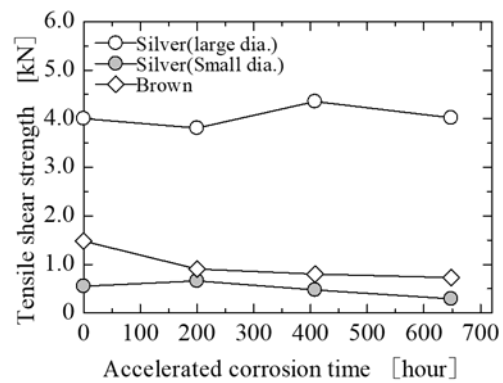


Figure 2-34. Relationship between acceleration time and shear load capacity of the weld zone

## Chapter 3. Micro-tremor measurement and health monitoring

### 3.1 Target structure

Microtremor measurement of rammed earth and stone masonry structures is useful tool to grasp not only their vibrational characteristics but also their static one. Moreover, finite element model can be modified by using their natural frequencies and mode shapes.

Microtremor measurement was carried out on **15** Rammed Earth houses [2] as listed in Table 3-1 and shown in Figure 3-1. Microtremor measurement was carried out on **20** Stone Masonry houses [3] as listed in Table 3-2 and shown in Figure 3-2.

Table 3-1. Overview of Rammed Earth buildings to be measured and list of measurement results

Name	Storey	Width [m]	Depth [m]	Height [m]	Thickness [m]	Natural Period[s]	
						Short	Longitudinal
Babesa House No.2	3	11.55	10.45	11.50	0.75	0.45	0.35
Pangrizampa Lhakhang	4	18.90	10.70	13.90	1.40	0.36	0.34
Wang Simu Lhakhang	2	9.40	8.60	5.83	0.77	0.21	0.21
Dolma Lhakhang	1	8.57	9.20	6.32	0.83	0.18	0.22
Kabesa Lhakhang	2	13.58	6.65	7.31	0.77	0.25	0.25
Nebab Goempa	3	13.25	9.40	9.72	1.10	0.30	0.39
Neyphung Lhakhang	2	20.30	14.36	11.80	1.17	0.42	0.40
Tsalumaphe Lhakhang	2	17.63	7.22	7.36	1.26	0.26	0.32
Sewla Lhakhang	2	11.51	9.76	8.70	0.73	0.35	0.27
Debsi House	3	13.60	6.70	8.00	0.73	0.22	0.22
U-RE-Short Specimen	2	8.10	5.40	6.83	0.60	0.20	
U-RE-Long Specimen	2	8.10	5.40	6.83	0.60	0.19	
R-RE-Short Specimen	2	8.10	5.40	6.83	0.60	0.16	
New-RE-Short Specimen	2	8.10	5.40	6.83	0.60	0.22	
Essuna?							

Table 3-2. Overview of Stone Masonry buildings to be measured and list of measurement results

Name	Storey	Width [m]	Depth [m]	Height [m]	Thickness [m]	Mortar	Natural Period[s]	
							Short	Longitudinal
Chhukha House	2	9.23	8.21	6.25	0.58	Mud	0.35	0.31
Dangdung House 1	4	8.64	9.07	10.7	0.83	Mud	0.29	0.29
Dangdung House 2	3	12.0	7.12	8.77	1.14	Mud	0.24	0.21
Dangdung House 3	2	6.28	5.62	5.61	0.63	Mud	0.21	0.21
Samcholing House 1	3	9.14	5.70	6.86	0.83	Mud	0.37	0.29
Samcholing House 2	2	8.21	5.63	5.73	0.60	Mud	0.24	0.21
SMM-U Specimen	2	8.10	5.40	6.83	0.60	Mud	0.19	0.20
Khasadrapchu House	2	14.1	9.19	5.68	0.54	Mud+Cement	0.15	0.16
SMC-U Specimen		8.10	5.40	6.83	0.60	Cement	0.11	
Ura House 1	2	11.08	9.14	5.19			0.18	0.17
Ura House 2	2	10.82	9.75	5.39			0.19	0.17
Ura House 3	2	11.55	9.50	5.70			0.20	0.18
Ura House 4	2	10.57	8.40	5.34			0.19	0.17
Ura House 5	2	11.87	9.67	6.03			0.21	0.19
Ura House 6	2	8.27	6.77	4.87			0.17	0.16
Ura House 7	2	9.77	8.05	5.19			0.18	0.17
Ura House 8	2	12.15	10.64	5.49			0.19	0.18
SMC-New Specimen		8.10	5.40	6.83	0.60	Cement	0.09	



(a) Babesa House No.2



(b) Pangrizampa Lhakhang



(c) Wang Simu Lhakhang



(d) Dolma Lhakhang



(e) Kabesa Lhakhang



(f) Nebab Goempa



(g) Neyphung Lhakhang



(h) Tsalumaphe Lhakhang



(i) Sewla Lhakhang



(j) Debsi House



(k) U-RE-Short Specimen



(l) U-RE-Long Specimen



(m) R-RE-Short Specimen



(n) New-RE-Short Specimen



(o) Essuna House 23



(p) Essuna House 30



(q) Essuna House 33

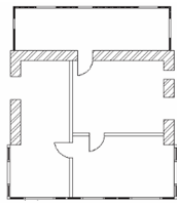


(r) Essuna House 35

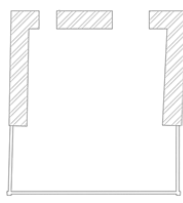


(s) Essuna House 38

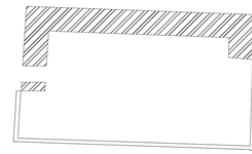
Figure 3-1. Target of Rammed Earth Structures (External view)



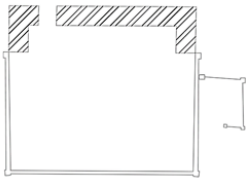
(a) Chhukha House



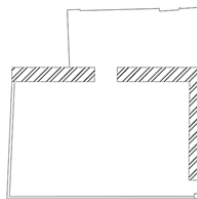
(b) Dangdung House 1



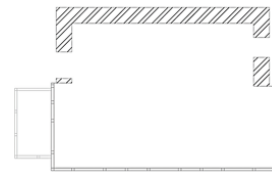
(c) Dangdung House 2



(d) Dangdung House 3



(e) Samcholing House 1



(f) Samcholing House 2





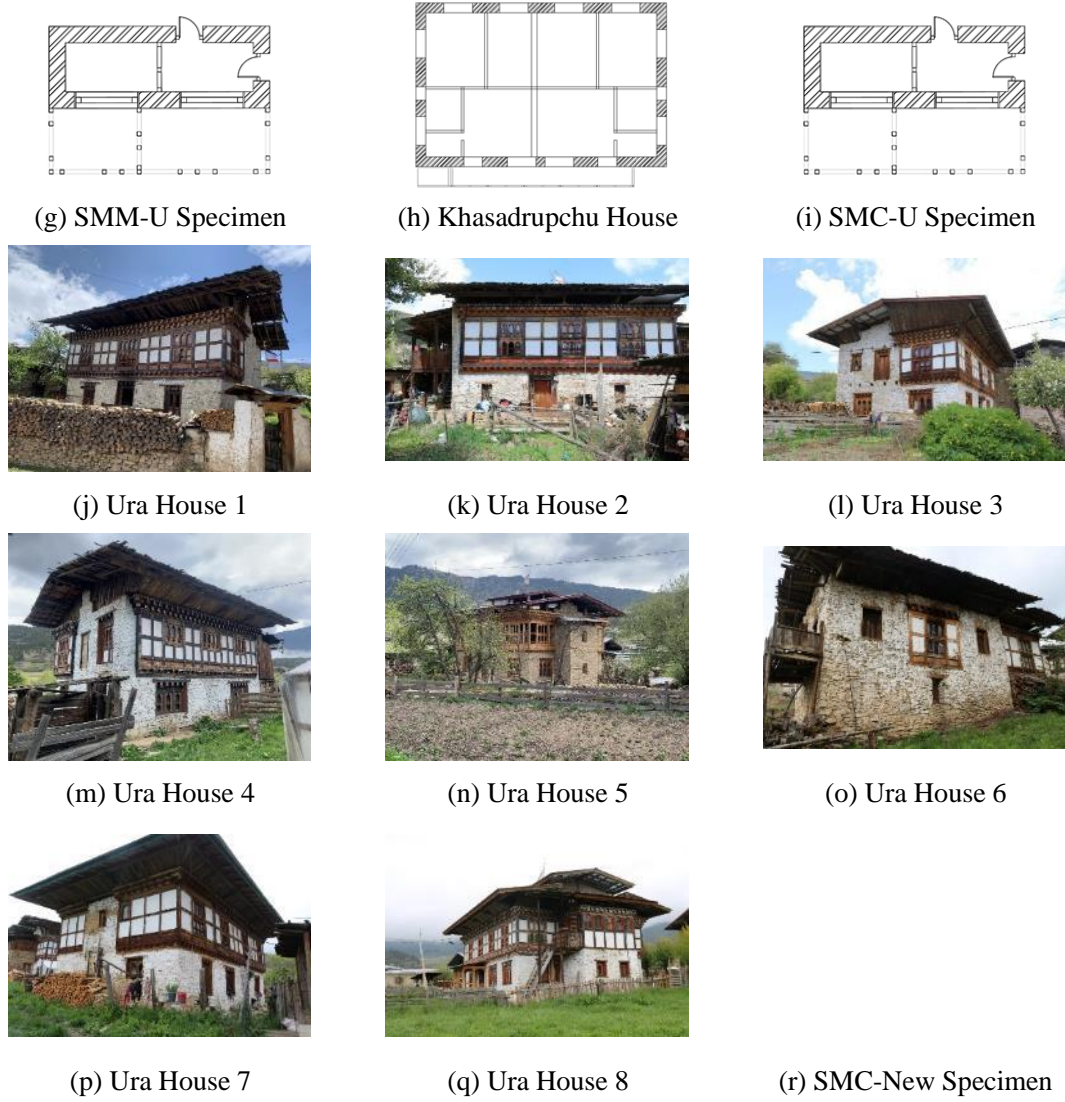


Figure 3-2. Target of Stone Masonry Structures (External view and abbreviate plan of the top floor)

### 3.2 Relationship between the heights of buildings and natural periods

Seismic force above the ground level is calculated as follows:

$$Q_i = W_i \cdot C_i \quad (3-1)$$

$$C_i = F_0 \cdot R_i \cdot A_i \cdot \alpha_h$$

where

$Q_i$ : the seismic shear force of point “ $i$ ” (the height from ground level)

$C_i$ : the seismic shear coefficient of point “ $i$ ”

$W_i$ : permanent load added to imposed load above point “ $i$ ” (+snow load, in heavy snow areas, as designated by the Designated Administrative Agency)

$F_0$ : the seismic zone factor (from 0.7 to 1.0). This value should be derived from seismography.

$R_i$ : vibration characteristic factor. This value should be derived from observation of surface layer of ground.

$A_i$ : vertical distribution factor

$$A_i = 1 + \left( \frac{1}{\sqrt{\alpha_i}} - \alpha_i \right) \frac{2T}{1 + 3T}$$

$T$ : Design Fundamental Natural Period. This value should be derived from experiment.

$$\alpha_i = \frac{W_i \text{ (Total permanent load added to imposed load above story } i \text{)}}{W \text{ (Total permanent load added to imposed load)}}$$

$\alpha_h$ : the standard shear coefficient

### 3.3 Relationship between the heights of buildings and natural periods

Figure 3-3 and Figure 3-4 show the relationship between the heights of Rammed Earth and Stone Masonry buildings where the microtremor measurements were conducted and the natural periods. The longitudinal direction and the short transversal direction are indicated separately in this figure. The natural periods are generally proportional to the heights of the buildings. From the statistical analysis of these data, Design fundamental natural period  $T$  will be derived, and then the vibration characteristic factor  $R_i$  will be calculated by taking into consideration with class of ground.

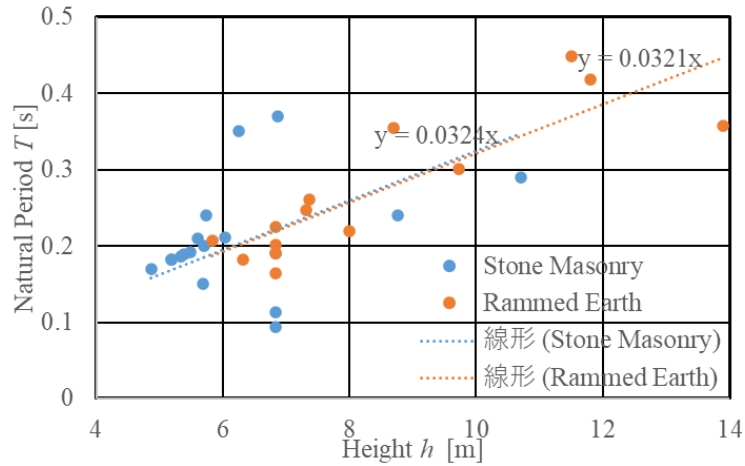


Figure 3-3. Relationship between natural periods and the heights of buildings

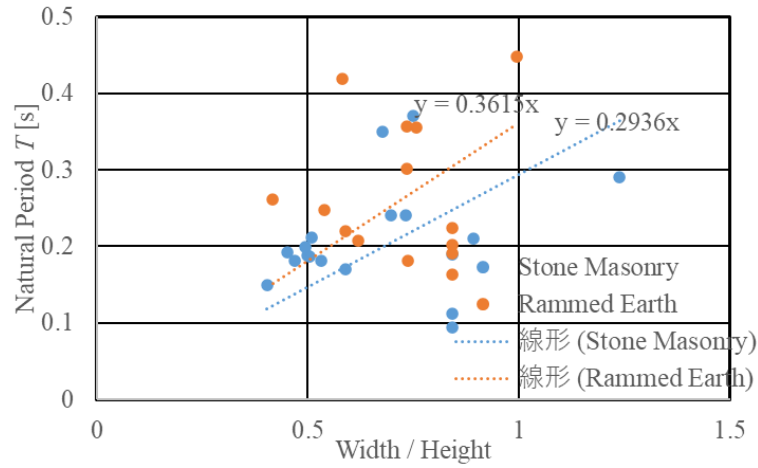


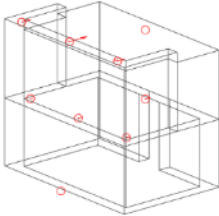
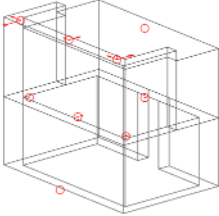
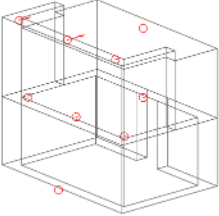
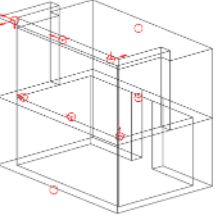
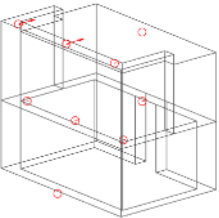
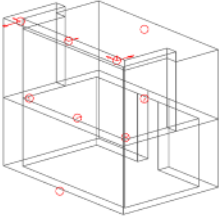
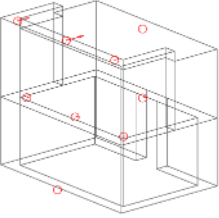
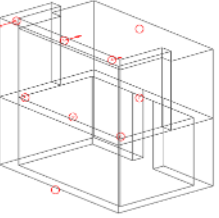
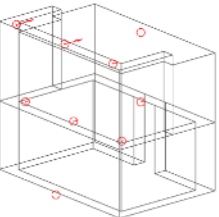
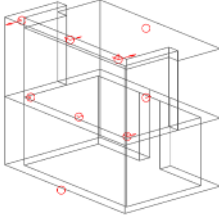
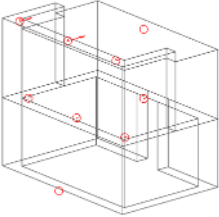
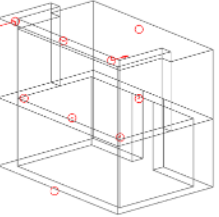
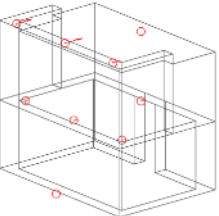
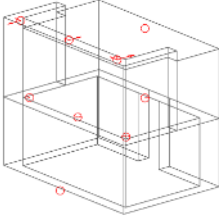
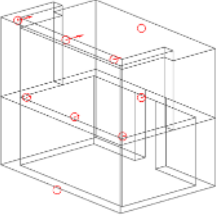
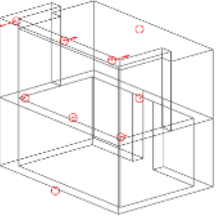
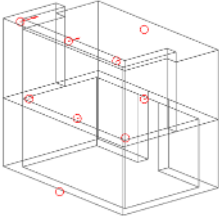
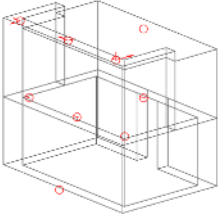
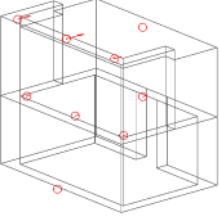
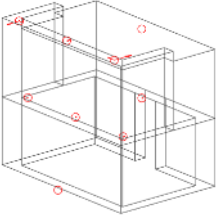
Figure 3-4. Relationship between natural periods and aspect ratio (Width/Height)

### 3.4 Change of Natural Frequencies during the Full-scale Static Tests

Table 3-3 lists the natural frequencies and mode shapes estimated from the measurement results for U-RE (unreinforced rammed earth) construction, New-RE (newly rammed earth) construction, U-SMC (unreinforced cement-mortar stone masonry) construction, and New-SMC (newly cement mortar stone masonry) construction [4]. It can be seen that the natural frequencies are higher for the stone masonry construction than for the rammed earth construction. The natural frequencies of the full-scale specimens are lower after loading up to a story drift angle of 1/500, but the natural frequencies are higher due to the increase in stiffness caused by the seismic reinforcement.

The natural frequencies of the New-SMC specimens are higher than those of the U-SMC specimens because of the stiffening effect of the reinforcing members. However, the New-RE construction has a lower natural frequency than the U-RE construction because the stiffening members make it difficult to compact the soil, resulting in a void between the stiffening members and the rammed earth construction, which reduces the stiffness of the rammed earth construction. This can be seen from the load-displacement curve of the full-scale experiment (Chapter 5).

Table 3-3. Overview of Stone Masonry buildings to be measured and list of measurement results

	Rammed Earth		Stone Masonry with cement mortar	
	1 <sup>st</sup> Mode	2 <sup>nd</sup> Mode	1 <sup>st</sup> Mode	2 <sup>nd</sup> Mode
Unreinforced before test	5.29 Hz 	7.48 Hz 	8.88 Hz 	14.14 Hz 
Unreinforced after test	4.64 Hz 	6.83 Hz 	7.52 Hz 	12.60 Hz 
Retrofited before test	6.03 Hz 	8.49 Hz 	9.21 Hz 	15.35 Hz 
Retrofited after test	5.22 Hz 	6.91 Hz 	6.30 Hz 	10.52 Hz 
New construction before test	4.45 Hz 	6.78 Hz 	10.63 Hz 	16.56 Hz 



### 3.5 Investigation of the vibration characteristics of the ground

Figure 3-5 and Figure 3-6 show the location of microtremor measurement about the ground. Figure 3-5 shows the ground 37.3m away from Babesa House No. 2 in the Thimphu suburb, and Figure 3-6 shows two nearby ground locations in the Tshenkher settlement of Talung village in the Haa Dzongkhag, where different earthquake damage occurred. In Figure 3-6, rammed earth buildings to the north, east, and south of the upper microtremor measurement location were damaged (indicated by red), while rammed earth structures to the north and south of the lower microtremor measurement location were not damaged (indicated by sky-blue). Instruments of microtremor measurement are shown in Figure 3-7 [1].



Figure 3-5. Location of microtremor measurement near the Babesa House No.2 (Google Earth Map)

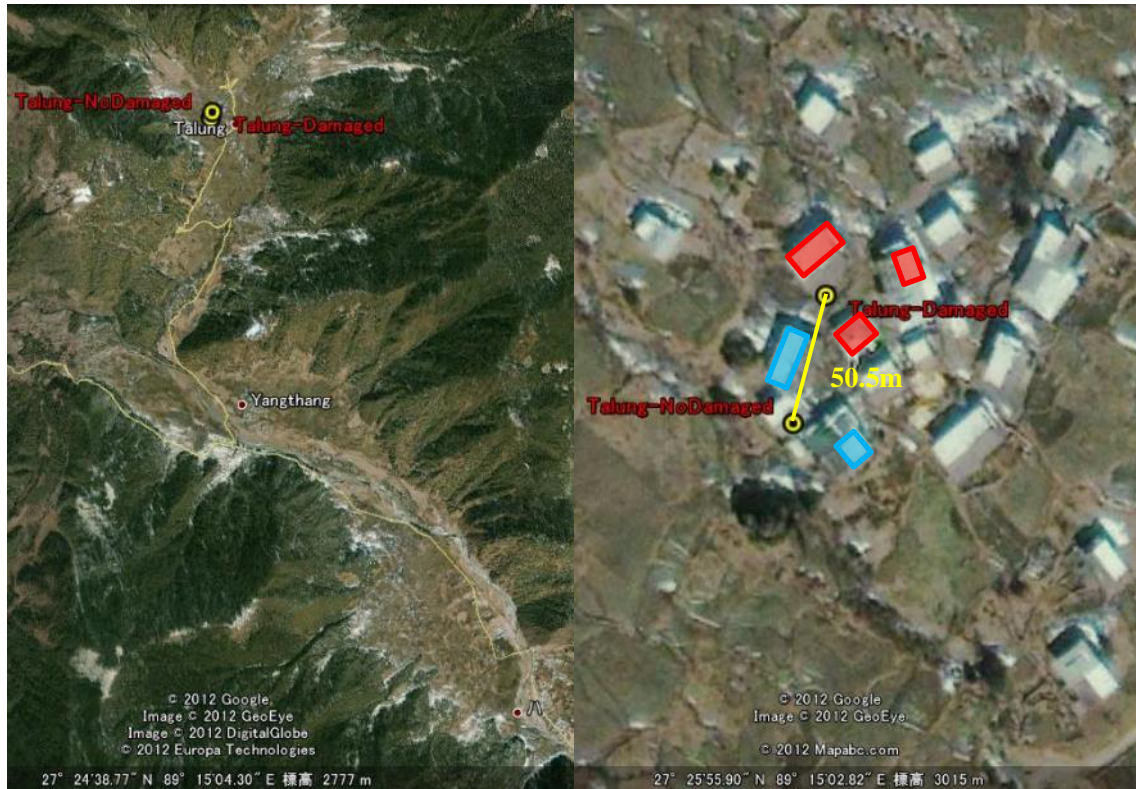


Figure 3-6. Location of microtremor measurement at Tshenkher settlement of Talung village in the Haa Dzongkhag (Google Earth Map)



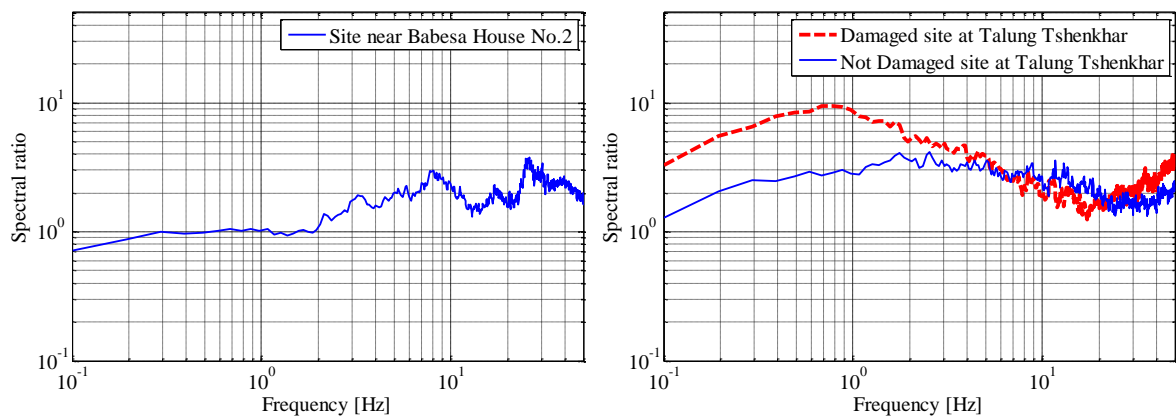
Figure 3-7. Microtremor measurement of ground at Tshenkher settlement of Talung village in the Haa Dzongkhag

The H/V spectral method is a method of estimating natural frequency of the ground from the spectral ratio of horizontal motion to vertical motion. The H/V spectral ratios of the measurement points on the ground of Figure 3-5 and Figure 3-6 are shown in Figure 3-8. From Figure 3-8 (a), wherein the peak occurs at a relatively higher frequency, it was deduced that the nearby ground of Babesa House No. 2 is relatively hard. On contrary, as shown in Figure 3-8 (b), in the Tshenkher settlement of Talung village in the Haa Dzongkhag, the ground where the larger amount of damage occurred (red curve) peaked at a lower frequency compared to the area that suffered no damage (blue



curve); it had soft ground that would easily vibrate. In other words, from the H/V spectral ratio, it was estimated that in the Tshenkher settlement of Talung village in the Haa Dzongkhag, the ground where a larger amount of damage had occurred had soft ground that easily vibrated, as compared to the area that suffered no damage; and the nearby ground of Babesa House No. 2 is harder than the ground of the Tshenkher settlement in the Talung village.

Results of microtremor measurement of the ground are related to the seismic zone factor  $F_0$ ; that should be derived from seismography, and vibration characteristic factor  $R_i$ ; that should be derived from the observation of surface layer of ground (class of ground).



(a) Babesa House No.2

(b) Tshenkher settlement of Talung village in the  
Haa Dzongkhag

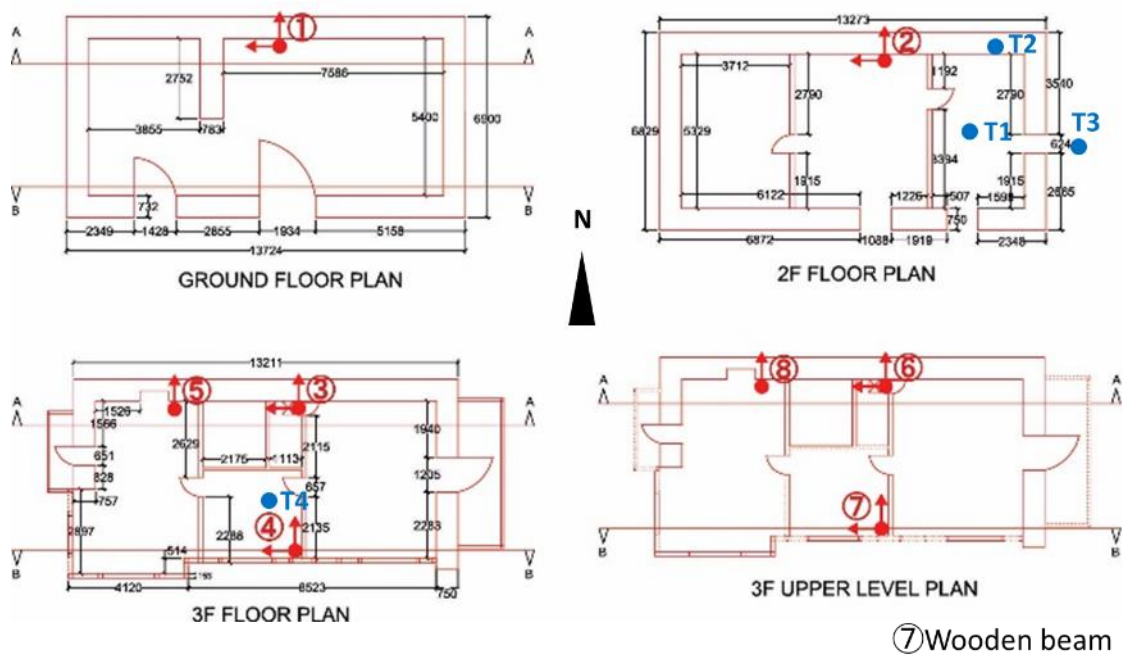
Figure 3-8. H/V spectral ratio of the ground

### 3.6 Health Monitoring

Monitoring is carried out on the Rammed earth building [5] and the stone masonry building.

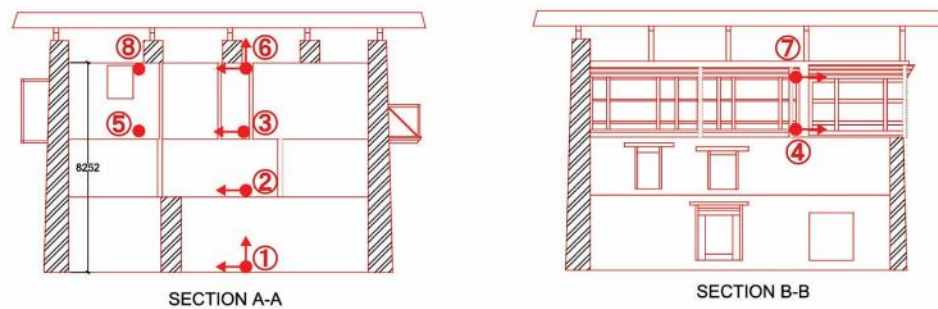


Figure 3-9. Monitoring of Rammed Earth building in Debsi, Thimphu



(a) Measuring position in plan

Accelerometer:  
 8 points  
 16 components  
 100 Hz  
 Thermocouple:  
 4 points  
 10 Hz



(b) Measuring position in section

Figure 3-10. Measuring position and measuring condition

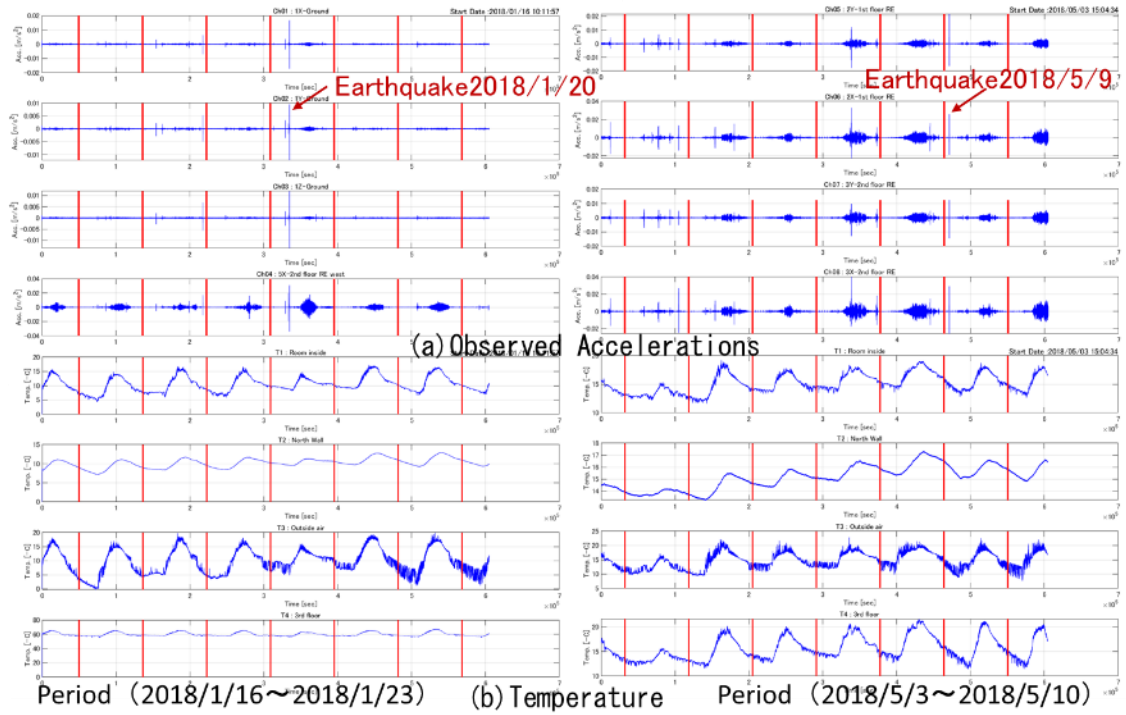


Figure 3-11. Observed Accelerations and Temperature

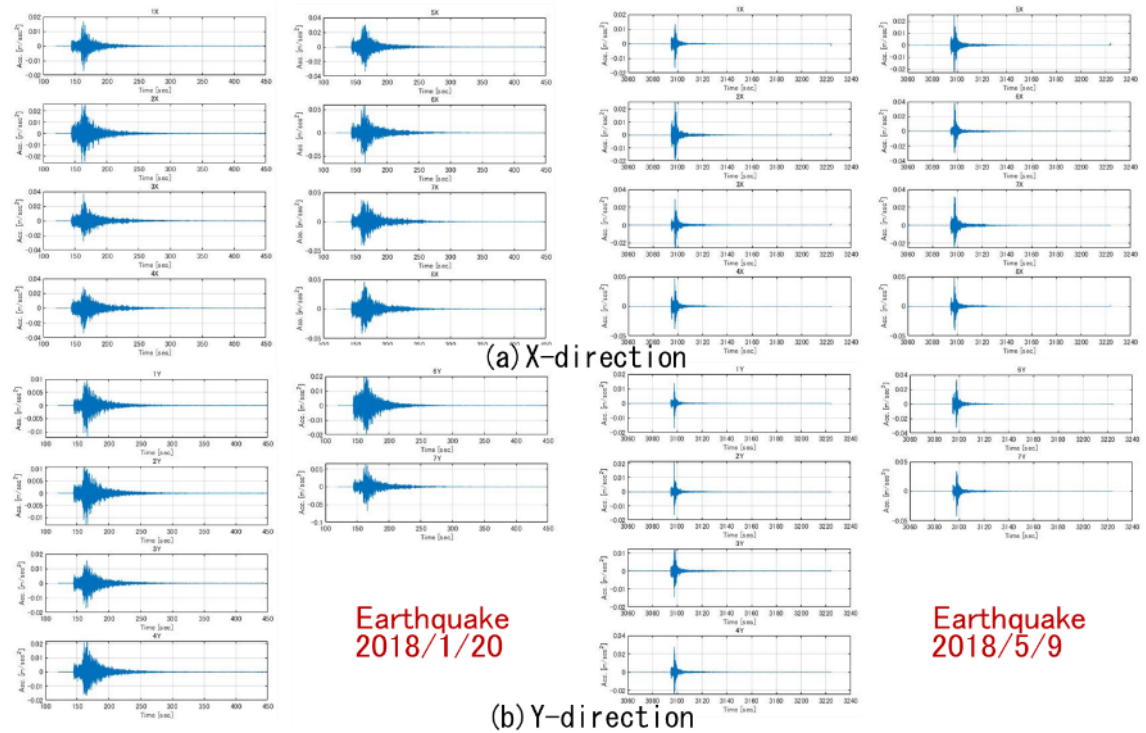


Figure 3-12. Observed Earthquakes

Table 3-4. Acceleration Amplification Ratio. Gal in parentheses.

	2018/01/20 Earthquake			2018/05/09 Earthquake		
	X-direction	Y-direction	Z-direction	X-direction	Y-direction	Z-direction
8:3FL ceilingNW	2.66 (4.55)	-	-	2.98 (4.95)	-	-
7:3FL ceiling beam※	2.37 (4.05)	5.54 (6.77)	-	1.93 (3.20)	2.46 (4.21)	-
6:3FL ceiling	3.91 (6.69)	1.59 (1.95)	1.72 (2.32)	2.29 (3.80)	1.96 (3.35)	1.55 (2.65)
5:3FL NW	1.98 (3.38)	-	-	1.55 (2.57)	-	-
4:3FL S	2.00 (3.43)	1.79 (2.18)	-	2.82 (4.69)	1.62 (2.78)	-
3:3FL	2.16 (3.69)	1.41 (1.72)	-	1.76 (2.91)	0.84 (1.44)	-
2:2FL N-Wall	1.53 (2.63)	1.08 (1.32)	-	1.56 (2.59)	1.27 (2.17)	-
1:GFL	1.00 (1.71)	1.00 (1.22)	1.00 (1.35)	1.00 (1.66)	1.00 (1.71)	1.00 (1.70)

※ Accelerometer was set on wooden beam

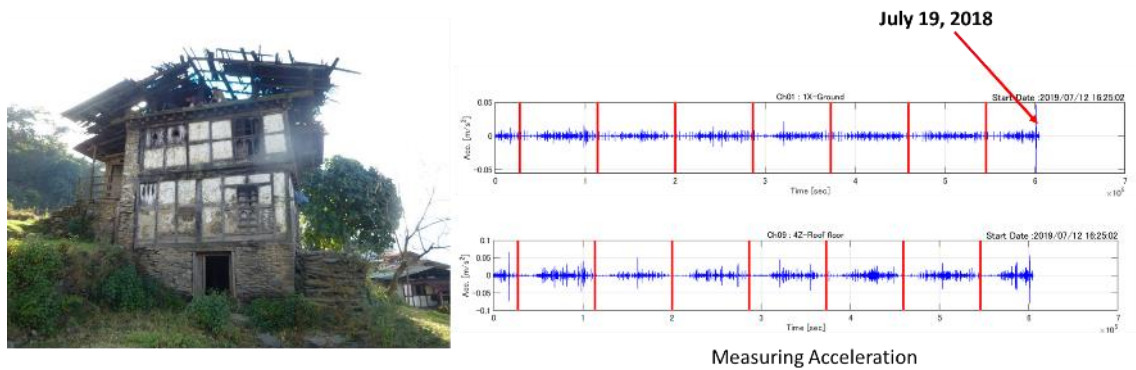


Figure 3-13. Monitoring of Stone Masonry building in Samcholing, Trongsa

## Chapter 4. Element Tests

### 4.1 Static element test on rammed earth walls

#### 4.1.1 Material and specimens

A total of 12 and 13 RE wallettes ( $500 \times 500 \times 110 \text{ mm}^3$ ) are tested in compression and shear, respectively. The considered parameters for both the test analysis are: i) Drying period (3 and 12 months) and ii) Layer thickness (50 mm and 100 mm). The soil used for the present study is reconstituted with a soil-sand ratio of 1:0.5 by volume [6]. The grain size distribution of the soil sample used has a particle size ranging from 0 to 10 mm. The specimen preparation involved manual compaction of moistened soil inside the formwork (Figure 4-2). The upper part of the layer achieved better compaction than the lower one. Further, 50 mm layer wallet achieved better compaction while honeycombs were found at the lowest level of the layer in case of 100 mm wallet, as seen in Figure 4-3. The formwork was removed immediately after completion of full specimen, allowing it to dry.





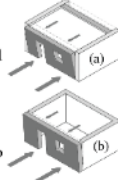

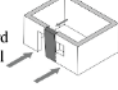

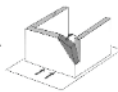

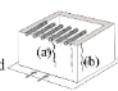



FAILURE AND MAIN POSSIBLE CAUSE	PHOTO INVENTORY
<b>Mechanism A_Out of plane wall collapse:</b> Toppling (horizontal arch) - Lack of floor/roof to wall connections - Long, thin and slender unbraced wall length 	
<b>Mechanism B_Out of plane wall collapse:</b> Buckling (vertical arch) - Lack of floor to wall or wall to wall connection - Rammed earth brittle behaviour 	 Photo: Wang et al. (2016)
<b>Mechanism C_Out of plane wall collapse:</b> Whole wall vertical overturning outward - Lack of adequate blocks overlapping - Lack of adequate horizontal plane junction between old and newly built walls - Lack of floor to wall connections at top 	 Photo: DCHS (2015)
<b>Mechanism D_Out of plane wall collapse:</b> Wall section vertical overturning outward - vertical openings alignment on the wall plane - Lack of floor/roof to wall connections 	 Photo: DCHS (2015)
<b>Mechanism E_Out of plane corner overturning:</b> Dislocation of corner - High stress concentrations due to poor roof anchoring and lack of uniform distribution of roof loads - Vertical corners cracks 	 Photo: DCHS (2015)
<b>Mechanism F_Local failures:</b> Vertical cracks - Floor or roof beams unthreading and hammering, due to displacement caused by horizontal seismic actions, (a) & (b) 	 Photo: DCHS (2015)
<b>Mechanism G_Local failures:</b> Lintel cracks - Asymmetric openings and inefficiency of lintel insertion in the wall masonry - Excessive openings dimensions 	 Photo: DCHS (2015)

Figure 4-1. Failure mechanism in RE buildings [7]





Figure 4-2: (a) Ramming to desired thickness; (b) Complete specimen

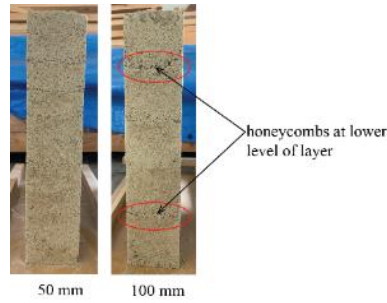


Figure 4-3. Compaction difference between the wallettes

A mesh-wrap strengthening technique was used as a possible strengthening measure. This technique involves the use of mesh, wrapped to the specimen surface on both facades using shear screws, and then plastered with 30 mm cement mortar (1 cement: 3 sand). The overview of mesh-wrap strengthening technique is shown in Figure 4-4.

Based on the identified test parameters, each specimen is named in “A-B-CD” format. Here, “A” denotes the unreinforced (U) or strengthened (R), “B” denotes the RE layer thickness either 50 mm or 100 mm, “C” indicates the test type compression (C) or shear (S) and “D” denotes the drying period in months either three months (3) or twelve months (12). For example, “U-100-C3” represents an unreinforced RE wallet with 100 mm layer thickness tested under compression loading after 3 months of the drying period. Additionally, for shear test, 0.1, 0.15, and 0.2 at end denote the vertical stress in MPa applied to the RE wallet. For example, “R-50-S12-0.2” stands for strengthened RE wallet with 50 mm layer thickness tested under shear loading after 12 months of drying period and subjected to vertical stress of 0.2 MPa.

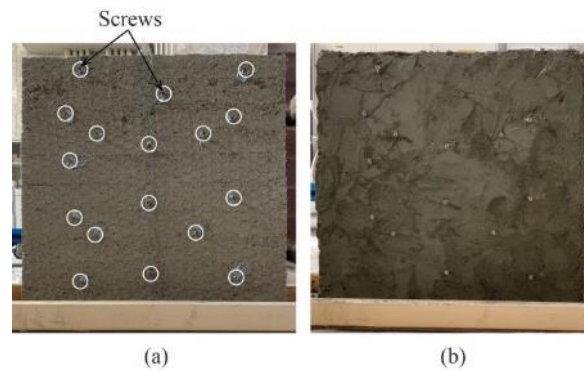


Figure 4-4. Strengthening details: (a) Fixation of mesh and screws; (b) Final view after plastering specimen



### 4.1.2 Test setup

The experimental setup for a compression test and a shear test is shown in Figure 4-5. For the compression test, two transducers and two PI-gauges were fixed at both faces of the wallet to measure the vertical displacement. A vertical load was applied through Universal testing Machine (UTM) until the failure of the wallet. For the shear test, seven transducers were fixed at different layers of RE wallet to record the horizontal displacement during the loading while two PI-gauges having a gauge length of 250 mm was placed diagonally to keep track of the cracks. Additional two PI-gauges were also fixed to record the vertical displacement. A slow and consistent horizontal load was applied until the failure through load cell (capacity 500 kN) with jack having a stroke of 150 mm while vertical stress is applied with UTM. The different normal stresses applied for each specimen were 0.2 MPa, 0.15 MPa and 0.1 MPa representing the first storey, the second storey and the roof respectively.

### 4.1.3 Results

Figure 4-6 shows the relationship between the compressive stress and strain for all RE wallettes tested under compression loading. Figure 4-7 shows the relationship between the shear load and displacement for all specimens tested under shear loading. It is observed that there is a steady increase in both compressive and shear strength as the drying period increases for both 100 mm and 50 mm layer wallettes. Furthermore, under both loading conditions, the strength for RE wallet with thinner layer 50 mm achieved better strength than the wallet with a thicker layer 100 mm. The higher strength in 50 mm layer wallet can be attributed to better compaction achieved comparing to the 100 mm layer wallet. The honeycombs in 100 mm layered wallet, seen in Figure 4-3, reduced the interface layer strength and thereby, affected the overall strength. From Figure 8, a gradual increase in shear strength is observed with an increase in vertical stress for all the RE wallettes with different layer thickness and drying periods.

A Mohr-Coulomb failure envelope is derived through a linear fit for shear strength values at various vertical stresses, as shown in Figure 4-8. The acquired cohesion ( $c$ ) and frictional angle ( $\phi$ ) values for 50 mm layer thickness are 0.01 MPa and 44.14 °, respectively. These values for 100 mm layer are 0.02 MPa and 30.96 °, respectively. The lower cohesion value and higher friction angle in 50 mm layer RE wallet are possibly influenced by rocking behaviour during the horizontal loading.

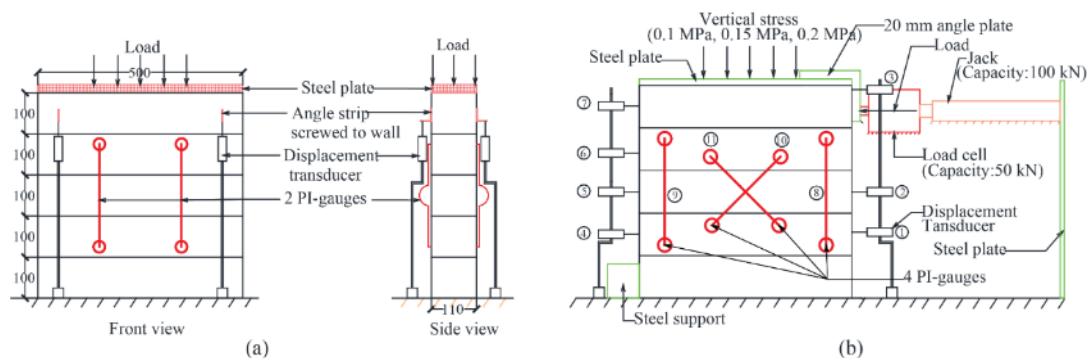


Figure 4-5. Test set up: (a) Compression test; (b) Shear test

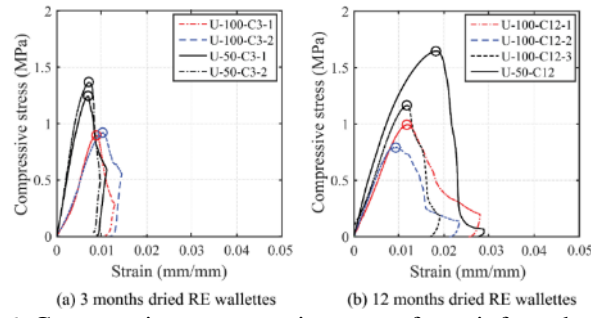


Figure 4-6. Compressive stress-strain curve of unreinforced wallettes

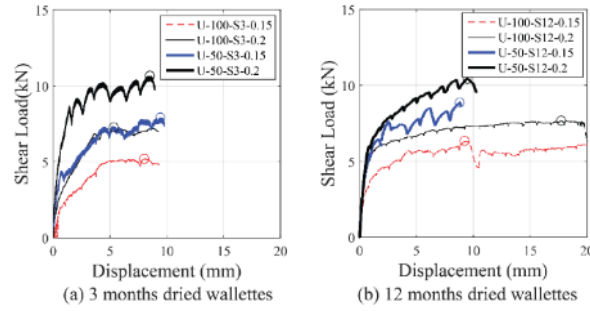


Figure 4-7. Shear load-displacement curve of unreinforced wallettes

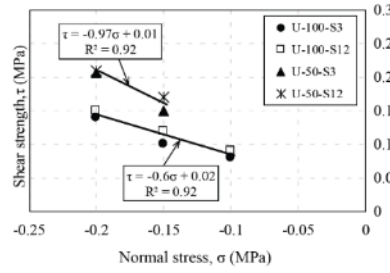


Figure 4-8. Shear strength of RE wallettes subjected to various vertical stresses

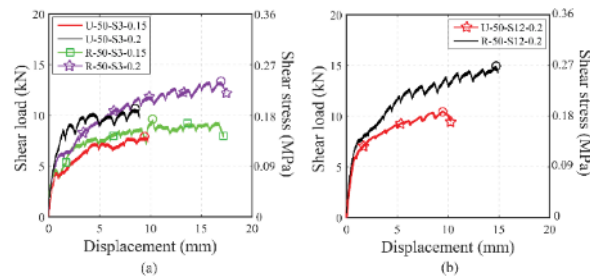


Figure 4-9. Shear load-displacement curve of strengthened wallettes: (a) 3-months dried; (b) 12-months dried

The proposed mesh-wrap strengthening method is effective in strengthening the RE wallettes tested under all considered parameters, as shown in Figure 4-9. The shear screws in Figure 4-4 were observed effective in controlling the mesh's delamination throughout the loading, and the delamination of mesh was observed only at the final failure.

Figure 4-10 and Figure 4-11 summarize the general failure observed for RE wallettes under compression and shear loading, respectively. A typical failure observed under compression loading includes inclined crack, curve like cracks at wallet sides, and vertical cracks. The typical failure observed under shear loading are, rocking usually observed in the initial loading with low vertical stress, diagonal crack, and the slip along the bed joint.

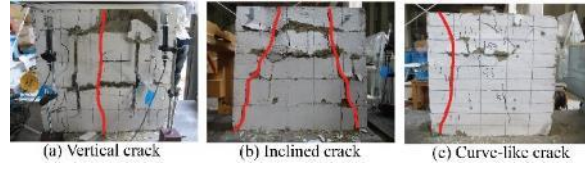


Figure 4-10. Typical failure patterns of RE wallettes observed under compression loading



Figure 4-11. Typical failure patterns of RE wallettes observed under shear loading

#### 4.1.4 Finite element modelling of RE walls subjected to in-plane loading

Two-dimensional finite element (FE) models are developed with finite element program DIANA following both the macro and micro-modelling approaches based on the total strain rotating crack model [8]. Rammed earth material was modelled with 650 eight-node quadrilateral isoparametric plane stress elements (CQ16M) and interface between the RE layers are modelled with 100 six-node interface elements (CL12I). For the strengthened wallet, the plaster element and steel wire mesh were modelled as single mesh composite element using eight-node quadrilateral isoparametric plane stress elements (CQ16M). The material properties for RE followed the experimental results of compression test while the interface element properties are calibrated based on the previous study [8]. The constitutive model for RE adopted an exponential softening for tensile behaviour, parabolic hardening with subsequent softening for compressive behaviour and Coulomb friction model for interface layers, as shown in Figure 4-12.

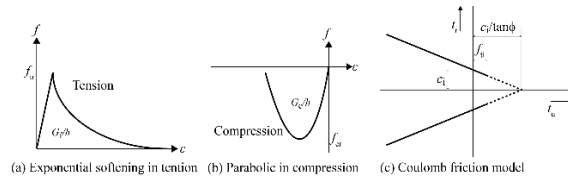


Figure 4-12. Material model adopted in FE Modelling

Table 4-1 presents the results from FE simulation and experimental program for both unreinforced and strengthened wallettes. The peak load values estimated by FE simulation are satisfactory with micro model predicting slightly lower than the macro model for both wall types. The macro model was able to simulate the diagonal shear failure; however, it failed to reproduce shear sliding observed for a few wallettes tested under lower vertical stress, as shown in Figure 4-13. Therefore, a micro model with interface layers needs to be considered for simulating the shear sliding and bed-joint opening. A sensitivity analysis is also carried out with variability in the mechanical properties of RE wallettes to understand their effect on shear strength. The result of the sensitivity analysis in Figure 4-14 shows that the compressive strength, tensile strength, and elastic modulus have the most significant influence on the shear behaviour of the RE wallettes. The interface of layer properties like cohesion, interface tensile strength, and friction angle was also found to have an effect, particularly when their values are reduced.

Table 4-1. Experimental and FE results

Specimen ID	Peak load $H_{\max}$ (kN)		
	Exp.	FE-macro	FE-micro
U-100-S12-0.2	7.69	7.32	6.57
U-100-S12-0.15	6.34	6.37	5.37
U-100-S12-0.1	4.73	5.51	4.39
U-50-S3-0.2	10.65	10.22	6.88
U-50-S3-0.15	7.91	9.22	5.61
R-50-S3-0.2	13.34	13.09	10.08
R-50-S3-0.15	9.61	11.63	8.78

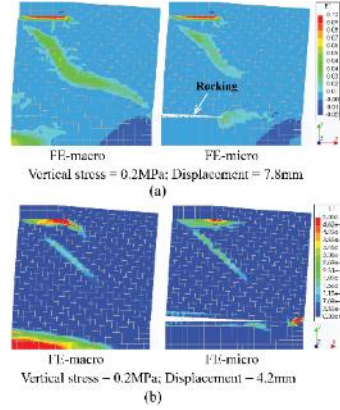


Figure 4-13. Failure mode observed in FE model: (a) unreinforced wallet; (b) Strengthened wallet

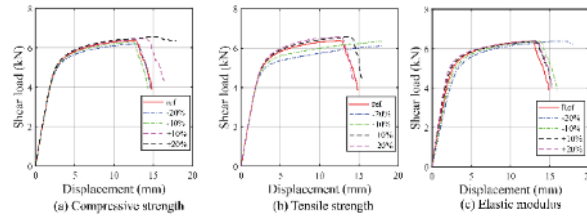


Figure 4-14. Results of sensitivity analysis

## 4.2 Pull-down test of rammed earth walls

### 4.2.1 Material and specimens

The damage assessment report showed that significant numbers of the building failed in out-of-plane [9]. Therefore, it is necessary to reinforce to prevent such failure, which is achieved through the pull-down test in this thesis. The thesis would contribute to the limited literature that aims to understand the out-of-plane behaviour of RE walls and strengthening technique for both existing and new RE construction.

The test program involved the preparation of five full-scale U-shaped specimens, namely unreinforced RE (U-RE), mesh-wrapped retrofitted RE (Mesh-RE), timber-framed retrofitted RE (Timber-RE), reinforced RE with reinforced concrete (RC) dowels and wedges (New-RE-A), and reinforced RE with RC posts, wedges, and band (New-RE-B). The specimen had a dimension of 5.4 m  $\times$  3.3 m  $\times$  2.4 m with a wall thickness of 0.6 m. The specimens Mesh-RE and Timber-RE aim to strengthen the existing structure, while specimens New-RE-A and New-RE-B aim to strengthen the new construction. The details of each specimen are presented in Figure 4-15. It should be noted that the details of specimen U-RE are not presented here for brevity and are similar to the rest of the specimens without the strengthening measures.

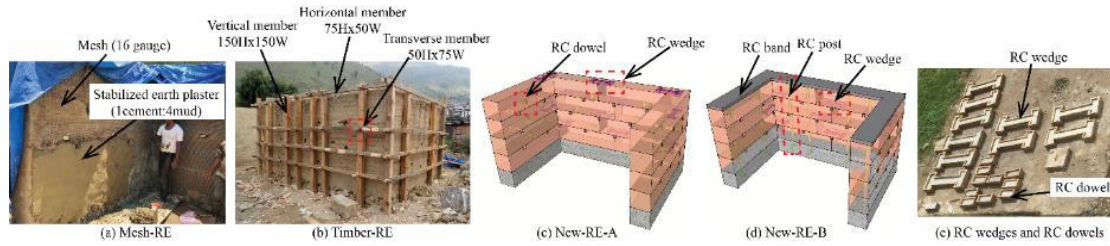


Figure 4-15. Specimen showing strengthening details: (a) Mesh-RE; (b) Timber-RE; (c) New-RE-A; (d) New-RE-B; (e) RC wedges and RC dowels inside formwork

#### 4.2.2 Test setup

Figure 4-16 shows the test setup and transducers' locations. The pull-down load was applied on facade wall with the backhoe of the crane to execute the overturning mechanism.

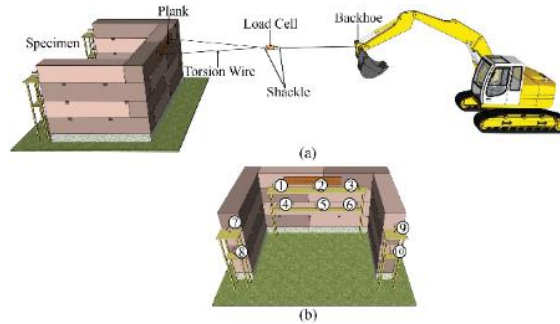


Figure 4-16. Test setup: (a) Overall view of pull-down test; (b) Location of transducers

#### 4.2.3 Results

The test results are presented in Figure 4-17 in terms of pull-down load versus displacement for all the specimens. The plot for pull-down load for each specimen is made against the displacements at the top level of facade wall (mean of sensor 1, 2, and 3) in Figure 4-17(a), mid-level of facade wall (mean of sensor 4, 5, and 6) in Figure 4-17(b) and top level of transverse walls (mean of sensor 7 and 9) in Figure 4-17(c). The pull-down loads for New-RE-A, New-RE-B, Mesh-RE, Timber-RE were 1.01, 3.19, 1.71, 1.09 times the unreinforced counterpart U-RE, respectively. The presence of RC dowel and RC wedges alone in the case of New-RE-A does not improve the wall's overall integrity. Therefore, its participation in improving strength is minimal. Therefore, it is necessary to provide RC posts starting from the foundation till the wall top and also RC band to connect the whole wall. From Figure 4-17(c), it is clear that the back section of the transverse walls showed deformation for New-RE-B, Mesh-RE, and Timber-RE, which attributes to the effectiveness of the proposed strengthening technique to unite facade wall and the transverse walls. Further, these strengthening measures were found to effectively control the wall's failure mode by preventing the total collapse of the front facade, as shown in Figure 4-18. Based on the contribution to the strength enhancement and controlling the failure mechanism, mesh-wrap technique, and RC components (posts, wedges and band) are considered for existing buildings and new construction of RE, respectively.

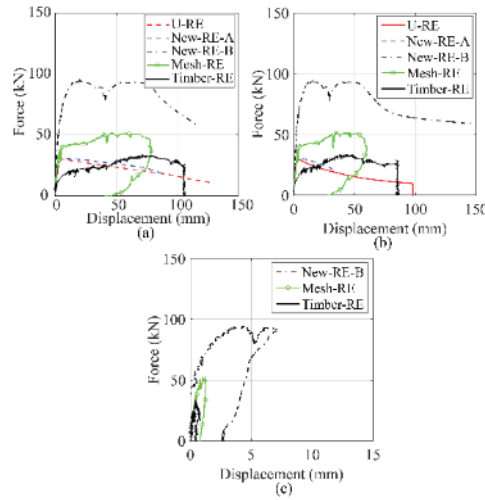


Figure 4-17. Load–displacement relationship at: (a) Top facade; (b) Mid facade; (c) Top of transverse wall



Figure 4-18. Final failure modes of all RE walls under out-of-plane loading

#### 4.2.4 Finite element modelling of RE walls subjected to out-of-plane loading

Only unreinforced wall (U-RE) is modelled with DIANA following both macro and micro modelling approaches. The three-dimensional macro-modelling approach uses the eight-node isoparametric solid brick elements HX24L (520 elements) to model the RE structure as a homogeneous continuum element. For the micro-modelling, the RE block interfaces were modelled using three-dimensional plane interface elements Q24IF (240 elements) between the faces of the HX24L brick elements (520 elements). The element size for meshing was kept at 300 mm. Even, in this case, the constitutive model adopted for the RE is based on the total strain rotating crack model, which describes both the tensile and the compressive behaviour of the material with one stress-strain relation.

The pull-down force vs. displacement acquired from the FE results are plotted together with the experiment result in Figure 4-19. It is observed that both FE-macro and FE-micro models well estimated the peak pull-down force. Furthermore, the experimentally observed failure mechanism was effectively predicted by the models, as shown in Figure 4-20. The failure is presented at two displacement levels: i) 2 mm at initial cracking phase and ii) 10 mm at final failure mode. Only FE-micro model was able to simulate the gap opening and delamination at the RE block interface.

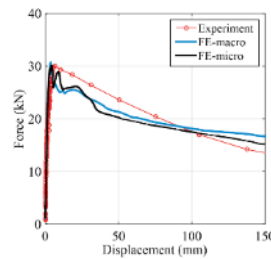


Figure 4-19. Experiment and FE results



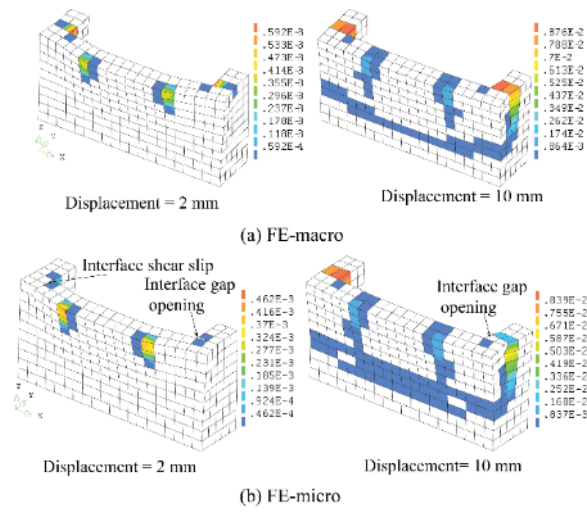


Figure 4-20. Failure modes observed for: (a) FE-macro; (b) FE-micro

## Chapter 5. Static loading tests

### 5.1 Test program

#### 5.1.1 Materials

##### (1) Rammed earth

The rammed earth (RE) material used in construction was from the nearby local site. The earth soil used for ramming included reddish-white clay with small pebbles. The grain size distribution of the RE used showed a particle size range of 0–10 mm. More details on the soil materials and particle size distribution can be found in Wangmo et al. [10]. For material characterization, RE cylindrical core samples were extracted from the test specimens using core drilling machine with diamond core bits for dry core drilling. In total, twelve of these cylindrical core samples for each specimen type were tested to measure compressive strength (ASTM C39) and splitting tensile strength (ASTM C496). Table 5-1 lists the properties of RE from material characterization.

Table 5-1. Material characterization of rammed earth block

Specimen	URE				RRE			
Unit	$\rho_b$	$f_c$	$f_t$	$E$	$\rho_b$	$f_c$	$f_t$	$E$
	(kg/m <sup>3</sup> )	(MPa)	(MPa)	(MPa)	(kg/m <sup>3</sup> )	(MPa)	(MPa)	(MPa)
Mean	1837	0.94	0.12	249	2024	1.65	0.17	389
Std. Dev.	33	0.12	0.02	58	13	0.15	0.03	55

##### (2) Timber

Wooden beam joists, 125 mm wide 150 mm deep of mixed conifer found in Bhutan, were used at the floor levels. The material properties for timber can be found in Shrestha et al. [11].

##### (3) Mesh retrofitting components

Two types of wire mesh were used, standard mild steel welded mesh as the main mesh, M-Mesh ( $\emptyset$  1.8 mm and 34 mm c/c spacing) and light and galvanized welded mesh as a lapping mesh, L-Mesh ( $\emptyset$  1.45 mm and 28 mm c/c spacing) at the corners and along the height of the walls. A cement plaster of ratio 1:3 (cement: sand) was applied to the RM wall substrate. The average compressive and tensile strength of the cement plaster was 17.38 MPa and 1.59 MPa, respectively. It should be noted authors are already working towards the use of stabilized mud plaster over the cement plaster in their future work. Cement plaster was chosen over stabilized mud plaster for the present work primarily due to limited curing time for the test specimen during the winter season. It may be argued that since the strength of cement plaster (30 mm thick) is far greater than that of rammed earth, there can be a



mechanical incompatibility between the two materials. It should be noted that the results reported are for the first set of series of planned tests, and authors will focus their future works to scrutinize these arguments further.

For material characterization of the retrofitting components, test coupons (Figure 5-1(a)) 200 mm long, 50 mm wide, and 30 mm thick were prepared for M-Mesh and tested under tensile loading with clevis type grip as shown in Figure 5-1(b). Figure 5-1(c) and Figure 5-1(d) show the test results for the tensile coupon tests. The plot in Figure 5-1(c) shows an initially high stiffness and drop in load at around 0.6–1 MPa stress representing the initial cracking in the mortar. Afterward, the stiffness reduces significantly, and the crack widens with further slip along the length of the coupon (Figure 5-1(d)). The authors will generalize these tensile test coupon tests to incorporate in the material characteristics for finite element modeling generation in their future works.

### 5.1.2 Test specimen details

#### (1) Prototype unreinforced rammed earth specimen (URE)

The full-scale tests were carried out on a prototype Bhutanese traditional house. The building represents a traditional residential house of Bhutan following the typical architectural pattern with limited openings at first floor level and a large opening on the second floor of the building's front facade. The prototype has a floor area of 8.1 m × 5.4 m as shown in Figure 5-2, with three rooms on each floor. The second floor level has a large opening in the front facade, termed as rabsey. The URE specimen was tested after four months of drying. The drying period was decided based on the authors' previous works [12].

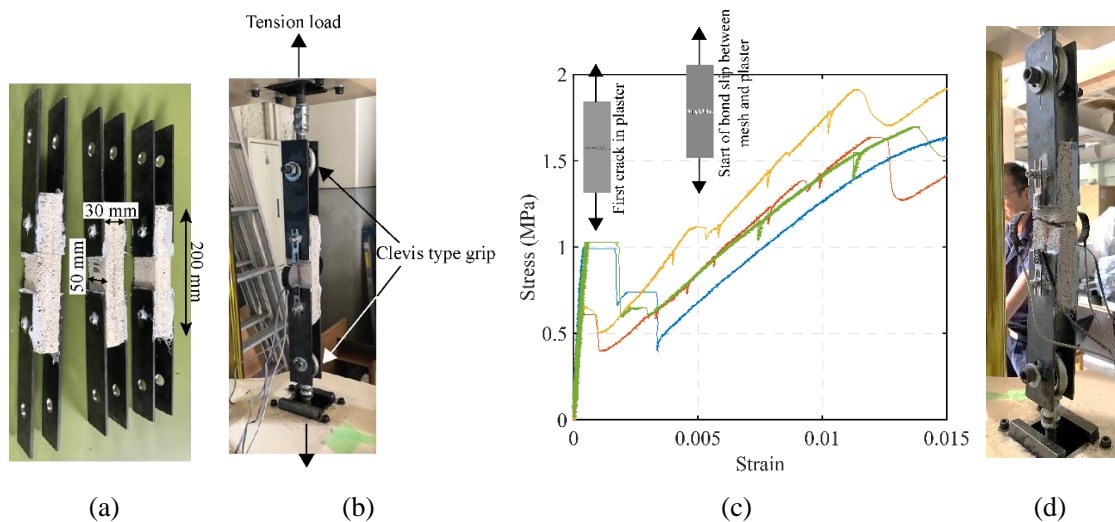


Figure 5-1. Material characterization tests for mesh retrofitting component: (a) Test coupons epoxy-bonded at the ends to steel plates, (b) Test set-up with clevis type grips, (c) Tensile stress versus strain plots for tensile coupon tests of M-Mesh, (d) Typical failure mode at the end of coupon test

## (2) Mesh-wrap retrofitting and retrofitted rammed earth specimen (RRE)

Figure 5-2 and Figure 5-3 show the details of the retrofitting works carried out on the specimen. It should be noted that the retrofitting was started after completion of the first series of tests on the unreinforced specimen, URE. Two types of wire mesh were used, standard mild steel welded mesh as the main mesh, M-mesh ( $\varnothing$  1.8 mm and 34 mm c/c spacing) and light and galvanized welded mesh as a lapping mesh, L-mesh ( $\varnothing$  1.45 mm and 28 mm c/c spacing) at the corners and along the height of the walls. A lapping length of 300 mm was provided in the vertical direction in regular intervals, while 600 mm lap was provided in the horizontal direction at the corners. First, the mesh was placed on the walls using U-hooks. This was followed by clamping of mesh to the walls using 12 mm diameter rods inserted through the jugging holes and bolted with nuts, as shown in Figures 2 and 3a. Finally, a 30 mm thick cement plaster (cement and sand at 1:3) was applied over the mesh. Prior to plastering, the wall's surface was pretreated using cement slurry (thin mix of cement and water). For the floor joist, X-bracing with timber of size 75mm $\times$ 75mm was provided to connect the floor joists. The X-bracings were bolted to the floor joists at the center and the ends. It should be noted that only the in-plane loaded walls (east and west elevations) were retrofitted as shown in Figure 5-2, with an extension of the L-mesh to the north and south elevations up to 600 mm. The RRE specimen was tested after three months of curing.

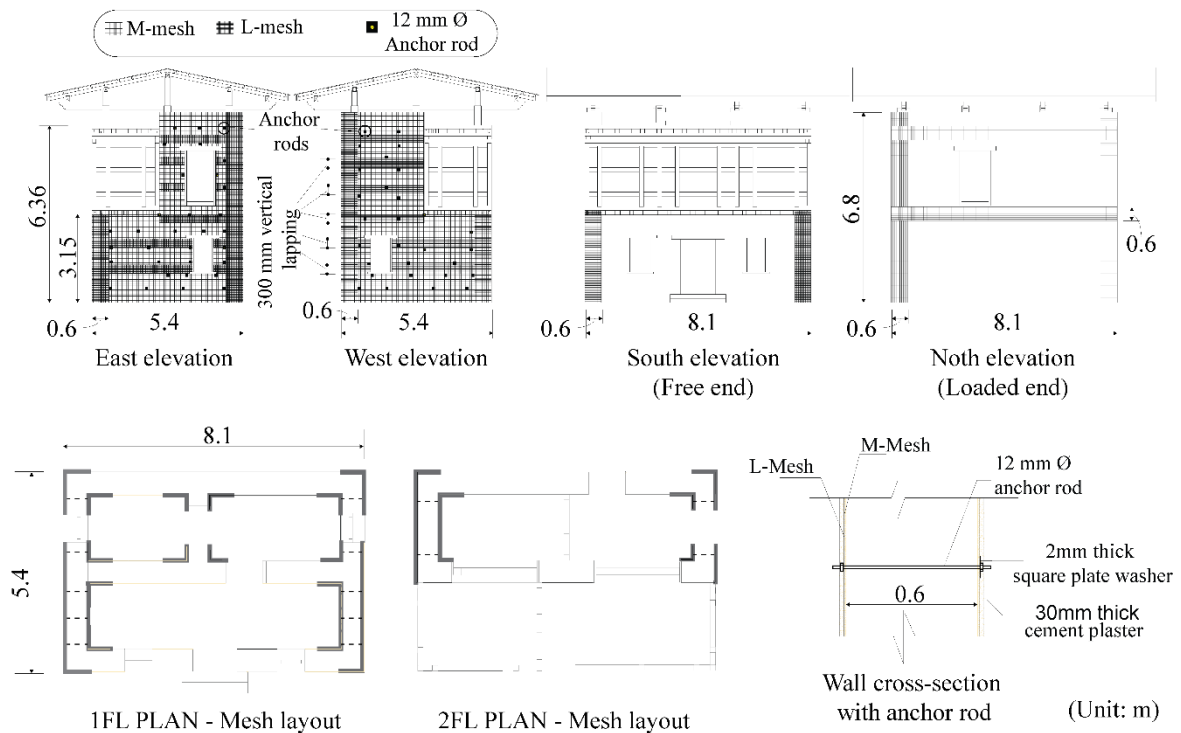


Figure 5-2. Prototype retrofitted rammed earth building specimen (RRE)

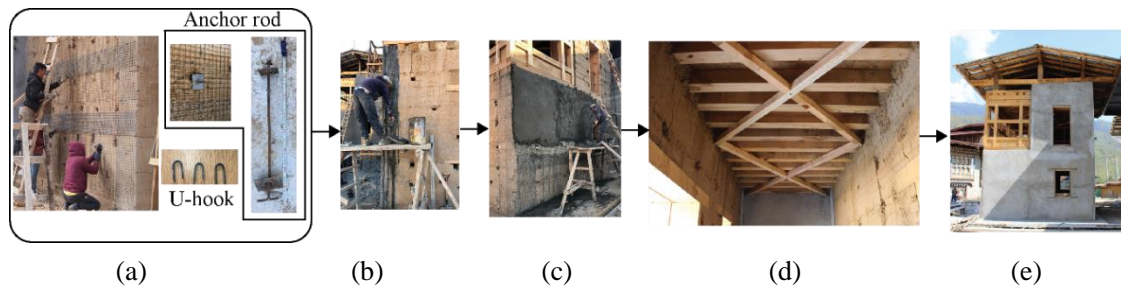


Figure 5-3. Retrofitting work process: (a) Placement and anchorage of mesh, (b) Application of cement slurry as pretreatment, (c) Cement plastering, (d) Wooden brace for floor rigidity, (e) Final specimen after retrofitting

### (3) Test set-up and instrumentations

The test set-up for the static test is illustrated in Figure 5-4(a). Two 1000kN capacity jacks were positioned at the second-floor level (2FL), and the other two of 500kN capacity were placed at the roof-floor level (RFL). One end of the jack was connected to the reaction wall through the built-up section and the other end to the test specimen's wall face through a 9.5 m long H-section. There were two 9.5 m long H-sections installed at each floor level, resting on support systems that allow them to slide along the support with the jacks. The static jack is a hydraulic system that was manually operated. The instrumentations are illustrated in Figure 5-4(a). The instrumentation involves load cells installed on hydraulic jacks to measure the applied forces. The displacement was measured using 14 displacement transducers: ten laser transducers (Keyence, IL-300) and four strain gauge type transducers (TML SDP-100C, SDP-50C) at three different levels (base, 2FL, and RFL) of the test specimen both at the loading and the free side. A multi-channel dynamic strainmeter DS-50A was used for data logging with the LAN interface setting. The data sampling rate was set at 100 Hz.

The static test loading protocol involved the displacement controlled loading with control over the drift in the building. Each floor level of the specimen was subjected to displacement controlled loading to a specified target storey drift value, followed by observation of cracks and damages to the building. Here, the storey drift ratio,  $\theta$ , is the ratio of the lateral displacement to the floor height. Cracks and damage observations were done at the storey drift ratios of: 1/2000, 1/1000, 1/750, 1/500 for the prototype unreinforced rammed earth specimen (URE). For retrofitted prototype specimen (RRE), in addition to above drift values, the building was subjected to storey drifts of 1/250, 1/150, 1/100, and 1/75. It should be noted that the loads applied in each storey levels, 2FL and RFL, were displacement controlled through manual synchronization, maintaining the target storey drifts through the monitoring of the drift records at the real-time data logging system. Figure 5-4(b) shows the target and the actual storey drifts for the static test, and the actual loading history can be considered satisfactorily closer to the target drift. The load cell measurements and the absolute displacement readings were collected to draw the capacity curves for each test specimen.

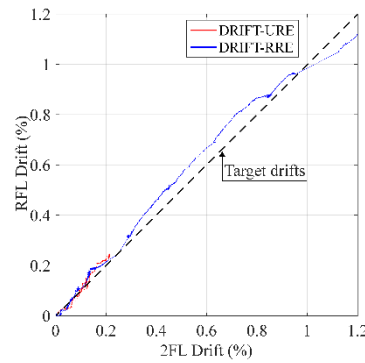
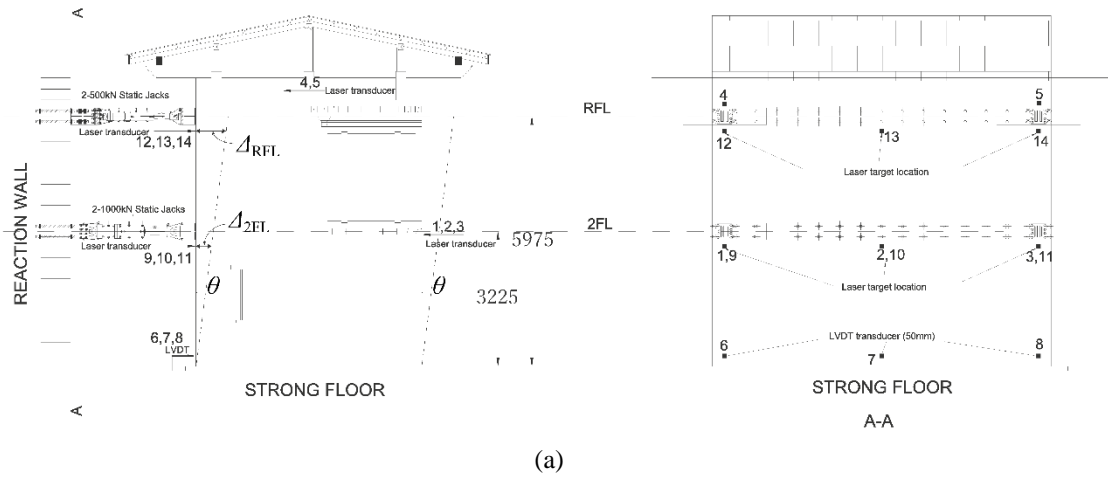


Figure 5-4: (a) Test set-up and instrumentation; (b) Actual and target storey drifts

## 5.2 Results and discussion

### 5.2.1 Micro-tremor measurements for dynamic characterization

Micro-tremor measurements for the test structures were made using three-component velocity sensor Model-2205B by Showa Sokki Corporation. The measurements were made to assess the vibrational characteristics of the prototype specimen before the test (no damage) and after the test (post damage) and also to study vibrational characteristics' changes after the retrofitting process. The data sampling was done at a frequency of 200 Hz with a recording time of 300 seconds. The measurements were done where the sensor pick-ups were placed at the 1FL, 2FL and RFL of the building specimen. Table 5-2 lists the first two natural frequencies for both the test specimens estimated using the Stochastic Subspace Identification (SSI) method. The first mode natural frequency for URE (before test) was 5.29 Hz, and this reduced to 4.64 Hz after the test with moderate damage at maximum storey drift of 1/500. Similarly, with the retrofitting measures, the first mode natural frequency increased to 6.03 Hz, which also subsequently reduced to 5.22 Hz after the test.

Table 5-2. Results from micro-tremor measurements

Specimen	Natural frequency (Hz)			
	Mode 1		Mode 2	
	Before test	After test	Before test	After test
URE	5.29	4.64	7.48	6.83
RRE	6.03	5.22	8.49	6.91

### 5.2.2 Capacity curve

Figure 5-5(a) shows the capacity curves in each floor correlated to the load cell readings for 2FL and RFL static jacks of both the prototypes, the unreinforced specimen, URE, and the retrofitted one, RRE. The presence of a large opening on the second floor and less contributions from the wall in load sharing means that the load recorded for the load cells in RFL was comparatively lower to the ones in 2FL. The first floor level, on the other hand, houses solid walls all around the building, hence, contributing to the higher load cell readings from the static jacks.

Figure 5-5(b) shows the global capacity curves with cumulative base shears of URE and RRE specimens. It should be noted that the drift ( $\theta$ ) shown in the capacity curves is the roof storey drift, defined as the absolute displacement of the roof (Sensors 12–14 in Figure 4a) divided by the height of the sensor from the ground. From the global capacity curves, the ultimate strength for RRE specimen (714 kN) was about 2.4 times URE specimen (294 kN), an increment of 420 kN. Further, the roof displacement for RRE (38.5 mm) at the maximum base shear was about 4.2 times for URE (9 mm).

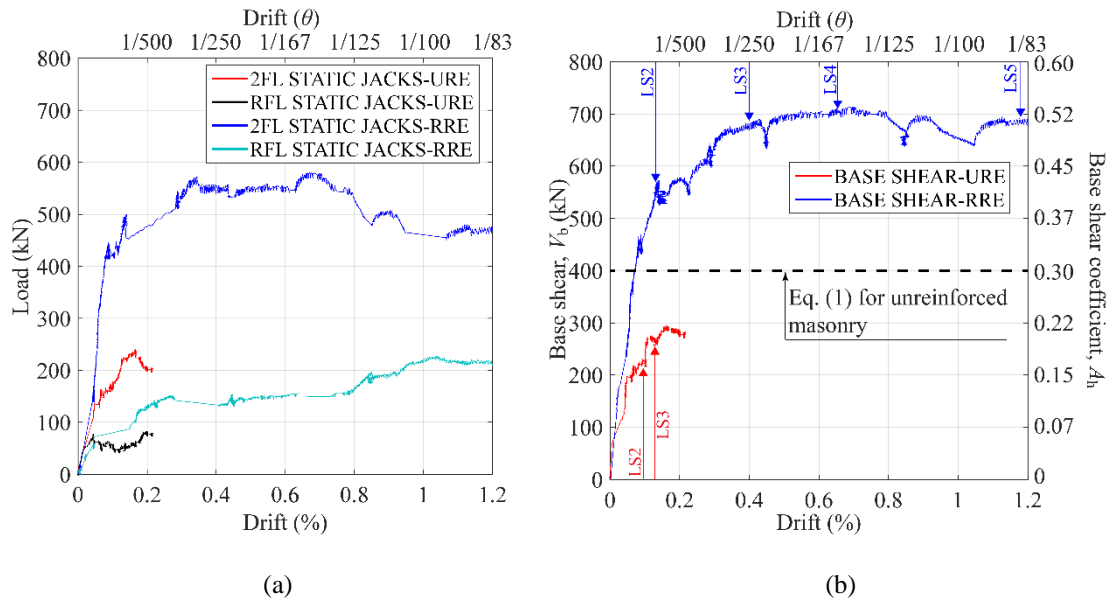


Figure 5-5: (a) Capacity curves in each floor for both prototype unreinforced and retrofitted specimens, (b) Global capacity curves for both prototype and retrofitted specimens

Indian Standard Code IS 1893 [13] provides simple formulations to compute design base shear

for unreinforced masonry in the Indian subcontinent, which was for comparison purposes in Figure 5b, represented by dotted lines. The design base shear [13] is given by:

$$V_b^D = A_h W_t \quad (5-1)$$

where,  $A_h$  is the design horizontal base shear coefficient given by  $(ZIS_a/g)/(2R)$  and  $W_t$  is the seismic weight of the building. Here,  $Z$  is the zone factor taken as 0.36 for very severe seismic zone,  $I$  is the importance factor taken as 1 for a residential building,  $S_a/g$  is the spectral acceleration coefficient taken as 2.5 for a natural time period of 0.2 second, and  $R$  is the response reduction factor taken as 1.5. The cumulative base shear of URE was below the design base shear value, and the retrofitted specimen RRE exceeded the design value by 1.8 times.

There were also significant enhancements in ductility and energy absorption for the RRE specimen, as shown in Table 5-3. Here, the energy absorption ( $\psi$ ) is given by the area under the global capacity curve until the ultimate base shear, and the corresponding top storey displacement. Ductility is the ratio of top storey displacement at the ultimate base shear to yield displacement. It should be noted that the results reported for unreinforced specimen URE were until the storey drift of 1/500; hence the values reported for energy absorption and ductility for URE can be slightly underestimated.

Table 5-3. Test results for the prototype unreinforced and retrofitted specimens

Specimen	Ultimate base shear, $V_b$ (kN)	Energy absorption, $\psi$ (kN–mm)	Ductility, $\mu$
URE	294	1813	3.4
RRE	714	22680	7.7

### 5.2.3 Damage observations and definition of the limit states

Real-time manual crack documentation was done during the test at the predefined target storey drift ratio through visual observations, and detailed drafting of the cracks was done at a later stage with the support of video recordings. The damage observations for the test specimens are illustrated in detail in Figure 5-6 for URE and Figure 5-7 for RRE. Here, cracks for in-plane walls in the loading direction are presented, and relatively smaller cracks for dispensable walls in out-of-plane are excluded.

The damage observed during the tests is also reflected in terms of limit states defined by five different predefined damage states, as illustrated in Table 5-4. The limit states in Table 5-4 are modified form of the same proposed by Nabouch et al. [14] for rammed earth walls, based on in-plane shear tests on individual rammed earth walls. Since the present study is on a full-scale structure, the proposed limit states are also more practical and representative of the actual real scale building.

Table 5-4. Limit states for rammed earth building

Limit states	Damage	Observations in the building
LS1	No damage	No crack observed
LS2	Slight damage	First appearance of cracks
LS3	Moderate damage	Cracks near openings (diagonal cracks); Toe crushing; First observation of fall of earth particles
LS4	Extensive damage	Extension of diagonal cracks; Extensive crushing; Extensive fall of earth particles
LS5	Total collapse	Excessive damage not economically reparable; Visible residual drift

## (1) Unreinforced rammed earth specimen (URE)

For URE specimen, the crack documentation, as illustrated in Figure 5-6 are presented for three storey drifts, 1/1000, 1/750 and 1/500. As reported earlier, the test was stopped at the drift of 1/500 for later retrofitting purposes and re-testing of the same building. The first few hair-line cracks originated near door openings and below the loading point in east elevation, and near lintel and jugshing holes of west elevation when the storey drift was up to 1/1000 (Limit state: LS2 Slight damage). For the storey drift of 1/750, there was an extension of cracks in the in-plane walls and new cracks were visible within the rammed earth blocks in 1FL (Limit state: LS3 Moderate damage). At 1/500 storey drift, there was a widening of the previous cracks and new inclined shear cracks within the rammed earth blocks in west elevation. A vertical crack about 1.5 m long also appeared at the far end in west elevation with some earth particles even falling (Limit state: LS3 Moderate damage). The authors felt the specimen experienced substantial damage to warrant its repair, and the test was stopped at this point since the main aim was to retrofit this building for re-testing purposes.. There was a negligible increment in cumulative base shear for URE specimen with further increment in drift. Therefore, based on authors' observations, limit state of LS4 representing "Extensive damage" will possibly occur for URE at storey drift of 1/250, which may not allow effective retrofitting of the specimen.

## (2) Retrofitted rammed earth specimen (RRE)

The crack documentation for RRE specimen is illustrated in Figure 5-7 for six different storey drift levels with their corresponding damage states defined. There were no cracks observed up to storey drift of 1/1000 (Limit state: LS1 No damage). At storey drifts of 1/750 and 1/500, hairline cracks started to appear near the lintels of openings. There were also numerous small vertical cracks below the rabsey opening corner, and horizontal cracks also initiated in both floor levels (Limit state: LS2 Slight damage). It should be noted that all the cracks were hairline cracks up to this load level. For storey drift of 1/250, there was widening and extension of previous cracks at the corner of rabsey opening and clear vertical cracks at the far end from the loading point. There was also crack due to toe crushing near the base of

the south face (Limit state: LS3 Moderate damage). At storey drift of 1/150, there were extensive cracks and slight spalling of plaster (Limit state: LS4 Extensive damage), with a clear long horizontal crack along the sill level, possibly the lapping region of the mesh. The previous cracks kept extending for storey drift of 1/100, followed by extensive spalling of plaster above the door opening (2FL) and also near the window opening (1FL). There was also plaster crushing at the toe near the base of the south face (Limit state: LS4 Extensive damage). At storey drift of 1/75, the cracks opened up significantly wide, and these relatively wide cracks were extending over the whole length of the wall. The spalling of plaster continued, and clear rocking of the entire building was visible. A sharp splitting sound possibly due to the dislocation of timber components was heard. Furthermore, the building also showed clear residual drift post the release of load. Based on the observation, this limit state level was defined as LS5 Near collapse. It should be noted that there was no delamination or separation of the mesh from the specimen throughout the whole test, showing the effectiveness of the anchor rods in keeping the mesh intact even at such adverse damage levels.



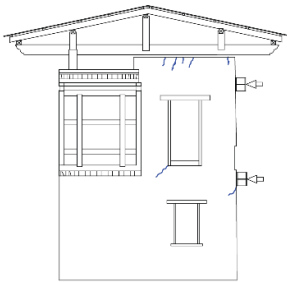
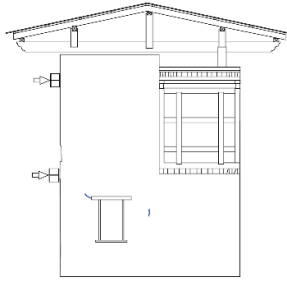
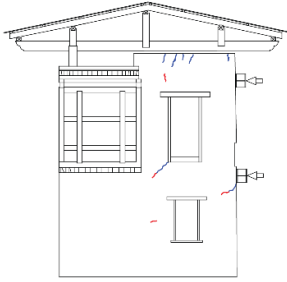
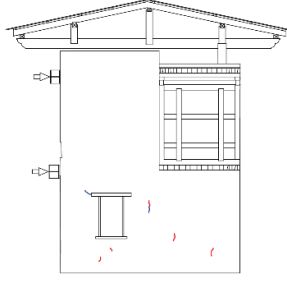
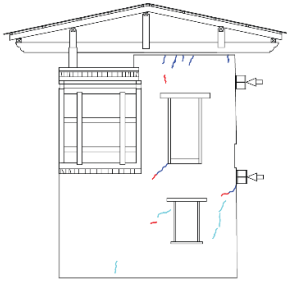
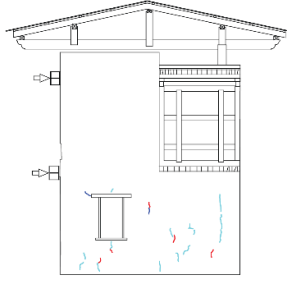
EAST ELEVATION	WEST ELEVATION	REMARKS
		<p><u>Storey drift, <math>\theta = 1/1000</math></u></p> <p>East elevation:</p> <ul style="list-style-type: none"> <li>- Small cracks below the door opening and the top RE block</li> <li>- Small cracks below the loading point in 2FL</li> </ul> <p>West elevation:</p> <ul style="list-style-type: none"> <li>- Small cracks above the window</li> </ul> <p><u>Limit state: LS2 Slight damage</u></p>
		<p><u>Storey drift, <math>\theta = 1/750</math></u></p> <p>East elevation:</p> <ul style="list-style-type: none"> <li>- Extension of the cracks below the door opening as well as below the loading point in 2FL</li> </ul> <p>West elevation:</p> <ul style="list-style-type: none"> <li>- Small cracks visible within the rammed earth blocks</li> </ul> <p><u>Limit state: LS3 Moderate damage</u></p>
		<p><u>Storey drift, <math>\theta = 1/500</math></u></p> <p>East elevation:</p> <ul style="list-style-type: none"> <li>- Widening and extension of the cracks below the loading point in 2FL</li> <li>- New cracks near the window opening</li> </ul> <p>West elevation:</p> <ul style="list-style-type: none"> <li>- Significant number of inclined cracks within the rammed earth blocks below 2FL originating from the Jugshing holes</li> <li>- A vertical crack about 1.5 m long appeared at the far end from loading point</li> </ul> <p><u>Limit state: LS3 Moderate damage</u></p>

Figure 5-6. Crack evolution for unreinforced rammed earth (URE) specimen at different load levels and their respective limit states

EAST ELEVATION	WEST ELEVATION	REMARKS
		<p><u>Storey drift, <math>\theta = 1/750</math></u></p> <ul style="list-style-type: none"> <li>- Hairline cracks near the window openings for both East and West elevations</li> <li>- Cracks near the corner of rabsey opening in West elevation</li> </ul> <p><u>Limit state:</u> LS2 Slight damage</p>
		<p><u>Storey drift, <math>\theta = 1/500</math></u></p> <ul style="list-style-type: none"> <li>- Extension of the previous cracks</li> <li>- Horizontal crack in both floor levels</li> <li>- Hairline vertical crack at the far end near South elevation</li> </ul> <p><u>Limit state:</u> LS2 Slight damage</p>
		<p><u>Storey drift, <math>\theta = 1/250</math></u></p> <ul style="list-style-type: none"> <li>- Extension and widening of previous cracks</li> <li>- New crack at the corner of rabsey opening</li> <li>- New vertical crack near the South elevation</li> <li>- Crack due to crushing near the base of South face</li> </ul> <p><u>Limit state:</u> LS3 Moderate damage</p>
		<p><u>Storey drift, <math>\theta = 1/150</math></u></p> <ul style="list-style-type: none"> <li>- Widening of previous cracks</li> <li>- Extensive cracks around the openings with slight spalling of plaster</li> <li>- Horizontal cracks along the sill level (lapping region)</li> </ul> <p><u>Limit state:</u> LS4 Extensive damage</p>
		<p><u>Storey drift, <math>\theta = 1/100</math></u></p> <ul style="list-style-type: none"> <li>- Deformed shape of the building was visually observed</li> <li>- Extensive spalling of plaster above the door opening and also near the window opening</li> <li>- Plaster crushing at the toe near the base of South face</li> </ul> <p><u>Limit state:</u> LS4 Extensive damage</p>
		<p><u>Storey drift, <math>\theta = 1/75</math></u></p> <ul style="list-style-type: none"> <li>- Large widening of already opened cracks</li> <li>- The previous cracks were extending towards the loading point</li> <li>- Spalling of the plaster continued</li> <li>- Rocking of the whole building was visible</li> </ul> <p><u>Limit state:</u> LS5 Near collapse</p>

Figure 5-7. Crack evolution for mesh-retrofitted rammed earth (RRE) specimen at different load levels and their respective limit states

## Chapter 6. Shaking table tests

### 6.1 Specimen configuration

The specimens were a reduced-scale prototype of a traditional Bhutanese masonry building, considering the limitation of the shaking table capacity. Eight specimens were constructed: four rammed earth and four stone masonry specimens, and two of each specimen were retrofitted. That is, there were two identical specimens, each with a different excitation direction in the short and long directions. The same materials were used in both the prototype and the models. The specimens were constructed by local craft men following the standard construction procedures in the Kingdom of Bhutan. All specimens were built on a steel base plate with a thickness of 10 mm and later fixed on a shaking table using bolts. The specimens were cured for 30 days after the construction was completed in the open air.

The specimens were geometrically reduced to a scale of 1:6. As shown in Figure 6-1, the two-storied prototype building had a floor area of 1350 mm × 900 mm, with a height of 580 mm for each floor. The wall thickness was 100 mm. After completing the construction, two of each specimen types were retrofitted with a mesh wrapping technique same as in the previous studies [15,16]. As shown in Figure 6-2, a hexagonal shaped chicken wire mesh having 0.4 mm diameter was used as the main material for retrofitting and anchored using nails. 10 mm thick cement plasters with a 1:3 cement–sand ratio were used to provide better bonding between the walls, mesh, and plasters.

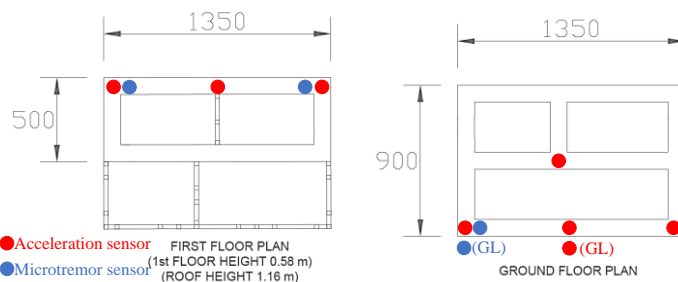


Figure 6-1. Plan of specimen



Figure 6-2. Reinforcement with wire mesh

### 6.2 Outline of shaking table tests

The shaking table tests were performed on two specimens at the same time: one was unreinforced, and the other was retrofitted. Comparisons were made on the spot, as shown in Figure 6-3. The response of the structure was measured using an accelerometer (STP-300S), and data logging was conducted using the National Instrument System (Signal Express). A total of 16 accelerometers were used to measure the response of the two specimens: eight on the unreinforced specimen and eight on the retrofitted specimen. For each specimen, one sensor was installed at the base, four at the second-floor level, and three at the roof level, as shown in Figure 6-1. The sampling frequency was set to 200 Hz.

The test was performed only in one direction of the specimens and was subjected to two types of dynamic excitations: sweep sine waves and real earthquake inputs. A sweep test was carried out with a low intensity (0.03 g) by gradually increasing the frequency from 1 Hz to 25 Hz to obtain the vibration characteristics of a model in the elastic range. Following the sweep test, a series of earthquake motions with increasing intensities were used for testing in the nonlinear range. The earthquake ground motion recorded in Thimphu, Bhutan, on September 12, 2018, was used as the input motion. The original wave was scaled following the similitude rule to suit the reduced-scale specimen [17], that is, the time axis of the original wave was reduced by a factor of  $6^{-3/4}$  times. The test was performed with increasing

the maximum acceleration of a ground motion from 0.2 g to 1.4g in 0.2 g increments. When the specimen was about to collapse, the test was stopped halfway through. Figure 6-4 and Figure 6-5 show the time history and acceleration response spectra of the input wave of 0.2 g.



Figure 6-4. Installation of specimen

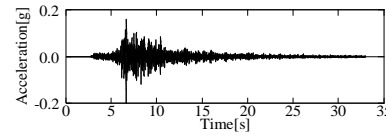


Figure 6-3. Example of time history

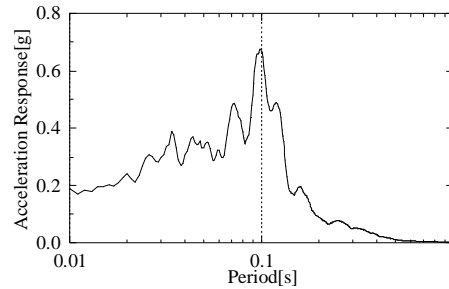


Figure 6-5. Example of acceleration spectrum

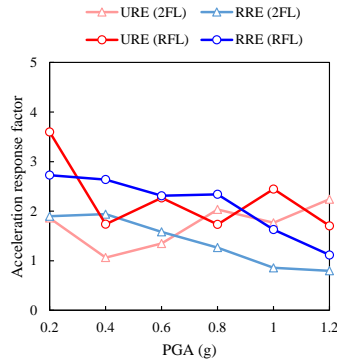
### 6.3 Results and discussion

The acceleration response factors at the floor and roof levels, crack patterns after tests in the short and long directions, and changes in natural frequencies are shown in Figure 6-6–Figure 6-9, respectively. The acceleration response factors were obtained from the average absolute peak acceleration response at each level by the absolute peak acceleration at the shaking table level. The measured values were used for the analysis after baseline correction and filtering using the band-pass filtering technique with cut-off frequencies of 1–50 Hz. Microtremor measurements of the specimens were performed before and after each test to understand the change in the vibration characteristics. The data loggers and sensors used for the measurement were GEODAS 15HRS and CR 4.5-2S velocity sensors, respectively. Microtremor waves were measured over 3 min by setting four sensors at each level in both directions, as shown in Figure 1, at a sampling frequency of 200 Hz. Subsequently, the measured values were divided by 20.48 s after filtering using the band-pass filtering technique with cut-off frequencies of 1–50 Hz. Those portions with less noise, such as those caused by traffic vibrations, were subjected to ensemble averaging and smoothing (Hanning Window:30). The obtained records were Fourier-transformed and the natural frequency of the specimen was estimated from the ratio of the Fourier spectra at each measurement point to that at the roof level.

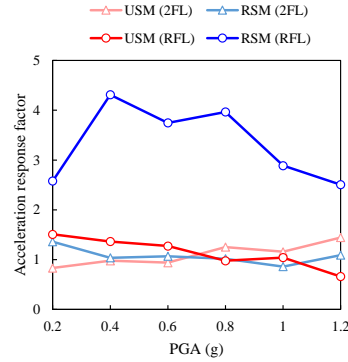
The test results for the short direction are as follows: After a nominal PGA of 0.8 g for an unreinforced rammed earth specimen (URE), the acceleration factor became almost the constant between the floor and roof level, and the natural frequency drastically dropped because of the occurrence of large horizontal cracks at the floor level and huge vertical cracks in the middle of the back wall (Figure 6-7 (a)). In a retrofitted rammed earth specimen (RRE), the acceleration factors gradually decreased at both the floor and roof levels and approached 1.0, owing to the effect of rocking. However, the natural frequency was almost constant, and there were few cracks although the nominal PGA increased in steps (Figure 6-7 (b)). In an unreinforced stone masonry specimen (USM), the acceleration factor was close to 1.0, at the roof level from the beginning owing to initial cracks, and the natural frequency was almost constant despite the gradual increase in the number of cracks. After a nominal PGA of 0.8 g, the natural frequency drastically decreased because of the occurrence of large horizontal cracks on both sides at the floor level (Figure 6-7 (c)). In a retrofitted stone masonry

specimen (RSM), the acceleration factors at the roof level and the natural frequency gradually decreased, although almost no cracks appeared on the surface of the exterior walls. (Figure 6-7 (d))

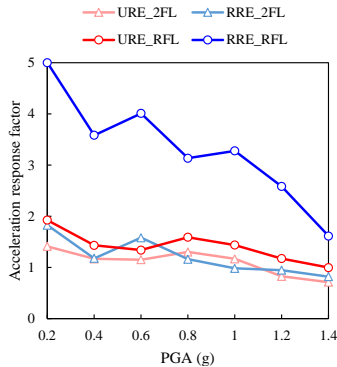
The test results for the long direction are as follows: In an unreinforced rammed earth specimen (URE), the acceleration factors at both the floor and roof levels were almost constant, and almost no cracks appeared on the surface of the exterior walls (Figure 6-8 (a)), although the natural frequency gradually decreased. In a retrofitted rammed earth specimen (RRE), the acceleration factors gradually decreased at the roof level owing to the effect of rocking, especially after a nominal PGA of 1.0 g. On the other hand, the natural frequency was almost constant, and there were few cracks on the surface of the exterior walls (Figure 6-8 (b)). In an unreinforced stone masonry specimen (USM), the acceleration factors at the roof level and the natural frequency gradually decreased until a nominal PGA of 0.6 g. However, after a nominal PGA of 0.8 g, these values began to increase owing to the prominence of wall vibration in the out-of-plane direction at the first floor (Figure 6-8 (c)). In a retrofitted stone masonry specimen (RSM), the natural frequency gradually decreased and there were few cracks on the surface of the exterior walls, even though the nominal PGA increased in steps (Figure 6-8 (d)).



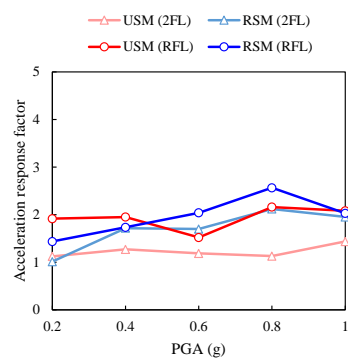
(a) Rammed earth (Short direction)



(b) Stone masonry (Short direction)



(c) Rammed earth (Long direction)



(d) Stone masonry (Long direction)

Figure 6-6. Acceleration response factor



(a) URE



(b) RRE



(c) USM



(d) RSM

Figure 6-7. Crack patterns after tests (Short direction)



(a) URE



(b) RRE

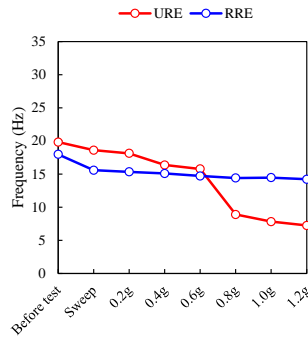


(c) USM

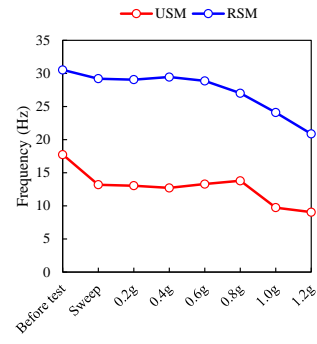


(d) RSM

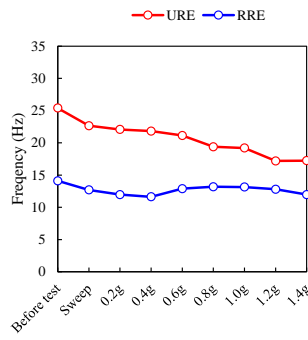
Figure 6-8. Crack patterns after tests (Long direction)



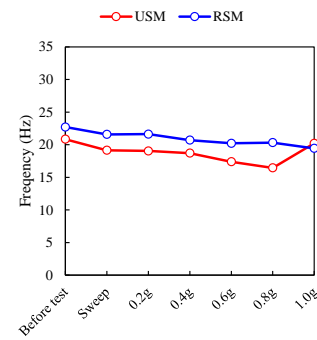
(a) Rammed earth (Short direction)



(b) Stone masonry (Short direction)



(c) Rammed earth (Long direction)



(d) Stone masonry (Long direction)

Figure 6-9. Change of natural frequencies

## Acknowledgements



## Referencies

---

- <sup>1</sup> M. Tomoda, K. Sato, M. Takashina, T. Ezura, Y. Samdrup, T. Aoki, H. Nakamura, Y. Tominaga, M. Miyamoto, Pema, “Report on Networking Core Centres Project for the Conservation of Traditional Buildings in the Kingdom of Bhutan 2012-2014 FY, Study on the Conservation of Rammed Earth Buildings in the Kingdom of Bhutan”, National Research Institute for Cultural Properties, Tokyo, Department of Culture, Ministry of Home and Cultural Affairs, Royal Government of Bhutan, pp.101-111, p.223, 2015.<sup>3</sup>
- <sup>2</sup> M. Miyamoto, T. Aoki, N. Takahashi, K.C. Shrestha, J.Y. Zhang, Study on earthquake resistance technology of composite masonry buildings in Bhutan (Part 6: Micro-tremor measurement of traditional rammed earth buildings), Summaries of AIJ Meeting, Structures-IV, pp. 913-914, 2018.7. [in Japanese]
- <sup>3</sup> M. Miyamoto, T. Aoki, N. Takahashi, K.C. Shrestha, S. Murai, S. Kanai, Study on earthquake resistance technology of composite masonry buildings in Bhutan (Part 15: Micro-tremor measurement of traditional stone buildings), Summaries of AIJ Meeting, Structures-IV, pp. 865-866, 2019.7. [in Japanese]
- <sup>4</sup> T. Aoki, H. Aoki, K.C. Shrestha, M. Miyamoto, N. Takahashi, Study on earthquake resistance technology of composite masonry buildings in Bhutan (Part 18: Microtremor measurement of full scale test specimens), Summaries of AIJ Meeting, Structures-IV, pp. 823-824, 2020.7. [in Japanese]
- <sup>5</sup> T. Aoki, M. Miyamoto, K.C. Shrestha, N. Yuasa, N. Takahashi, J.Y. Zhang, T. Aramaki, Study on earthquake resistance technology of composite masonry buildings in Bhutan (Part 1: Project summary and monitoring of traditional rammed earth building), Summaries of AIJ Meeting, Structures-IV, pp. 903-904, 2018.7. [in Japanese]
- <sup>6</sup> N. Yuasa, T. Aoki, T. Aramaki, M. Miyamoto, K.C. Shrestha, N. Takahashi, J.Y. Zhang, P. Wangmo, Study on earthquake resistance technology of composite masonry buildings in Bhutan (Part 2: Material strength of rammed earth), Summaries of AIJ Meeting, Structures-IV, pp. 905–906, 2018.7. [in Japanese]
- <sup>7</sup> P. Roberto, F. De Filippi, M. Bosetti, T. Aoki, and P. Wangmo, Influence of Traditional Building Practices in Seismic Vulnerability of Bhutanese Vernacular Rammed Earth Architecture, International Journal of Architectural Heritage, pp. 1–20, 2020, doi: 10.1080/15583058.2020.1785044.

- 
- <sup>8</sup> Miccoli, L.; Oliveira, D. V.; Silva, R.A.; Müller, U.; Schueremans, L. Static behaviour of rammed earth: experimental testing and finite element modelling. *Materials and Structures*, 2015, 48, 3443–3456, doi:10.1617/s11527-014-0411-7.
- <sup>9</sup> DCHS, Damage Assessment of Rammed Earth Buildings-After the September 18, 2011 Earthquake. Division for Conservation of Heritage Sites, Department of Culture, Ministry of Home and Cultural Affairs, Royal Government of Bhutan, 2011.
- <sup>10</sup> Wangmo, P., Shrestha, K.C., Miyamoto, M. and Aoki, T. Assessment of out-of-plane behavior of rammed earth walls by pull-down tests. *International Journal of Architectural Heritage* (2019) 13:273–287.
- <sup>11</sup> Shrestha, K.C., Aoki, T., Miyamoto, M., Wangmo, P., Pema, Zhang, J. and Takahashi, N. Strengthening of rammed earth structures with simple interventions. *Journal of Building Engineering* (2020) 29:101179.
- <sup>12</sup> Shrestha, K.C., Aoki, T., Miyamoto, M., Wangmo, P. and Pema. In-plane shear resistance between the rammed earth blocks with simple interventions: Experimentation and finite element study. *Buildings* (2020) 10:57.
- <sup>13</sup> Indian Standard 1893 Part 1. Indian Standard Criteria for earthquake resistant design of structures Part 1 General provisions and buildings, Bureau of Indian Standards, 5th edition, (2002).
- <sup>14</sup> El Nabouch, R., Bui, Q.B., Ple, O. and Perrotin, P. Rammed earth under horizontal loadings: Proposition of limit states. *Construction and Building Materials* (2019) 220:238-244.
- <sup>15</sup> Wangmo, P., Aoki, T., Shrestha, K. C., Miyamoto, M., Aoki, H., Kanai, S., Zhang, J., Takahashi, N., Yuasa, N., Murai S. and Shin S.: Study on earthquake resistance technology of composite masonry buildings in Bhutan Part 13: Full scale tests on composite masonry buildings: Unreinforced and mesh-wrapped rammed earth construction. *Summaries of Technical Papers of Annual Meeting, AIJ, Structures-IV*, 861-862 (2019).
- <sup>16</sup> Shrestha, K. C., Aoki, T., Miyamoto, M., Wangmo, P., Aoki, H., Kanai, S., Zhang, J., Takahashi, N., Yuasa, N., Murai S. and Shin S.: Study on earthquake resistance technology of composite masonry buildings in Bhutan Part 14: Full scale tests on composite masonry buildings: Mesh-wrapped stone masonry with mud mortar construction. *Summaries of Technical Papers of Annual Meeting, AIJ, Structures-IV*, 863-864 (2019).
- <sup>17</sup> Kagawa, T.: On the similitude in model vibration tests of earth-structures. *Proceedings of the Japan Society of Civil Engineers*, No.275, 69-77 (1977).